Journal of Geophysical Research: Atmospheres

RESEARCH ARTICLE
10.1029/2018JD028589

Diurnal Cycle of Precipitation and Cloud Clusters in the MJO and ITCZ Over the Indian Ocean

Brandon W. Kerns[1] and **Shuyi S. Chen**[2]

[1]Applied Physics Laboratory, University of Washington, Seattle, WA, USA, [2]Department of Atmospheric Sciences, University of Washington, Seattle, WA, USA

Key Points:
- Satellite and radar data show a nighttime rain max with noticeable differences between the MJO and ITCZ over the equatorial Indian Ocean
- The nighttime precipitation max in the ITCZ is more pronounced than in the MJO, which is associated with large long-lasting cloud clusters
- Radar data show a secondary afternoon rain max in the equatorial region when diurnal cycle of SST is $>$ 0.5 °C and wind speed is $<$5 m/s

Correspondence to:
B. W. Kerns,
bkerns@uw.edu

Citation:
Kerns, B. W., & Chen, S. S. (2018). Diurnal cycle of precipitation and cloud clusters in the MJO and ITCZ over the Indian Ocean. *Journal of Geophysical Research: Atmospheres*, *123*, 10,140–10,161. https://doi.org/10.1029/2018JD028589

Received 27 FEB 2018
Accepted 14 AUG 2018
Accepted article online 27 AUG 2018
Published online 19 SEP 2018

Author Contributions:
Conceptualization: Brandon W. Kerns, Shuyi S. Chen
Data curation: Brandon W. Kerns
Formal analysis: Brandon W. Kerns
Funding acquisition: Shuyi S. Chen
Investigation: Brandon W. Kerns, Shuyi S. Chen
Methodology: Brandon W. Kerns, Shuyi S. Chen
Resources: Shuyi S. Chen
Supervision: Shuyi S. Chen
Validation: Brandon W. Kerns, Shuyi S. Chen
Visualization: Brandon W. Kerns
Writing - original draft: Brandon W. Kerns
Writing – review & editing: Brandon W. Kerns, Shuyi S. Chen

Abstract Satellite observations of the diurnal cycle of precipitation and cloud clusters show a dominant nighttime maximum over the tropical Indian Ocean, similar to other basins. The nighttime maximum is associated with the relatively long lifetime of large convective systems that initiated during the afternoon when the sea surface temperature (SST) reached its diurnal maximum as first showed in Chen and Houze (1997, https://doi.org/10.1002/qj.49712353806). Shipborne and island-based radar data from Dynamics of the Madden-Julian Oscillation show distinct characteristics of the diurnal cycle in the equatorial region and Intertropical Convergence Zone (ITCZ). A secondary afternoon precipitation maximum occurs under light surface winds ($<$5 m/s) when the diurnal cycle of SST is large (0.5–1.7 °C) in the equatorial region during the suppressed phase of the Madden-Julian Oscillation (MJO). The afternoon maximum was from short-lived convective systems with rain rates $>$10 mm/hr. In contrast, during the active MJO and in the ITCZ, the secondary afternoon maximum is mostly absent as the surface winds were generally $>$5 m/s and reduced afternoon SST warming to less than 0.5 °C. The Tropical Rainfall Measurement Mission Multiplatform Precipitation Analysis does not resolve the secondary afternoon maximum in heavier rain rates from short-lived small systems, but it suggests a more pronounced night-morning maximum in the ITCZ than in the MJO. Infrared 208-K cloud cluster analysis show that this difference in the morning maximum was due to the greater number of long-lasting, large convective systems ($>$~200 km in diameter) persisting into the morning in the ITCZ.

1. Introduction

The ultimate source of diurnal variability in the atmosphere is incoming solar radiation. Over land, heating of the land surface leads to destabilization of the atmosphere and an afternoon maximum on most days. However, the ocean has several orders of magnitude greater heat capacity than land. Indeed, a nocturnal/early-morning rain maximum has been measured on ships and small islands and is a well-known feature of the tropical oceans (Gray & Jacobson, 1977). Nevertheless, the daytime insolation maximum often leads to an afternoon maximum of SST, which would be expected to enhance convection by destabilizing the lower troposphere (Matthews et al., 2014). Chen and Houze (1997, hereafter CH97) show that while infrared (IR) cold clouds (e.g., $<$208 K) have an early morning maximum, there is a weak afternoon maximum in small convective cloud systems, which is most evident during suppressed periods. Furthermore, during the active periods, the largest, long-lived cloud systems associated with the morning maximum have their origins in smaller systems, which initiated in the afternoon. Using Tropical Rainfall Measurement Mission (TRMM) Precipitation Radar (PR), Nesbitt and Zipser (2003) showed that there is an afternoon maximum in small convective systems over the sea, while the nocturnal maximum is associated with large organized mesoscale convective systems.

Several mechanisms have been proposed to contribute to the nocturnal rainfall maximum over the sea. Differences in infrared radiative cooling between large, organized mesoscale convective systems (MCSs) and their clear or partly cloudy surroundings can make the cloudy region positively buoyant compared to the clear regions, leading to a maximum just before sunrise (Gray & Jacobson, 1977). Note that in disturbed conditions with large convective systems, the diurnal cycle of rain can peak several hours before the maximum in the extent of cold clouds (Janowiak et al., 1994). Therefore, not all of the cloud radiative forcing translates into rain. This forcing mechanism disappears soon after sunrise when the tops of the clouds are heated by solar radiation (Cox & Griffith, 1979; Webster & Stephens, 1980). Another favorable factor at night is higher relative humidity, which would tend to reduce the impact of entrainment (Dai, 2001; Dudhia, 1989; Tao et al.,

1996). Another perspective has been provided by CH97, which found that long-lived convective systems tend to be triggered in the afternoon and go through their natural life cycles, reaching their mature stage with largest areal extent in the night and morning hours. The life cycle of the organized mesoscale convective systems plays a key role in determining the diurnal cycle of cold cloud tops and rain. Furthermore, the next day's convection at the same location can be suppressed due to the more stable postconvection boundary layer, resulting in strong nocturnal maxima every second night, which is referred to as *diurnal dancing*.

Near large landmasses, land and sea breeze circulations play a large role in forcing an offshore nocturnal maximum of rainfall, especially where the land breeze converges with the prevailing flow (Ichikawa & Yasunari, 2006; Qian et al., 2013; Williams & Houze, 1987). An alternative mechanism for enhancing nocturnal convection offshore is that a diurnal gravity wave may be triggered by the afternoon warming, especially over mountainous terrain. The gravity wave would then propagate offshore triggering convection over the sea at night (Mapes et al., 2003; Mori et al., 2004). Nevertheless, for the central Indian Ocean (IO) the influence of land on the diurnal cycle of rainfall is expected to be negligible.

Satellite and in situ rainfall data suggests that even over the open ocean, the amplitude and phase of the diurnal cycle is not uniform. Yang and Slingo (2001) noted that the amplitude of the diurnal cycle harmonic of brightness temperature was similar over the western Pacific and the Indian Ocean; however, the diurnal cycle harmonic of IR satellite estimated rainfall was ~2 mm/day (~30%) greater over the western Pacific, which had the greatest diurnal rain amplitude among the tropical oceans. Furthermore, the phase of the diurnal harmonic had significant regional variability. Brightness temperature tended to have a noticeably earlier peak in climatologically disturbed regions like the Intertropical Convergence Zone (ITCZ) and the monsoon trough, although this was not the case for the estimated rainfall. The estimated rainfall harmonic amplitude was somewhat noisy, but in general the Indian Ocean and west Pacific both had morning maxima. Bowman et al. (2005) compared the diurnal cycle harmonics of Tropical Atmosphere Ocean (TAO) moored buoy data and TRMM Microwave Imager (TMI) over the tropical Pacific Ocean. The locations near the equator tended to have smaller amplitude and earlier peak compared to the locations 5–10° away from the equator, which correspond with the climatological ITCZ. The degree of regional variability and related processes of the tropical open ocean diurnal cycle, away from large land masses, have not entirely been determined.

In addition to regional variability, the diurnal cycle of precipitation is modulated by large-scale circulations like the Madden-Julian Oscillation (MJO). Because convection over the equatorial IO is largely controlled by the MJO, we refer to the equatorial region in context of the MJO in this study. Using TRMM Multisatellite Precipitation Analysis (TMPA) data, Tian et al. (2006) found that the MJO mainly modulates the amplitude of the diurnal cycle but not its timing. Notably, they did not find any indication of an afternoon maximum over the sea using TMPA data. However, more recent studies have found that both the diurnal cycle phase and amplitude are modulated by the MJO. The diurnal cycle amplitude is enhanced and phase delayed by ~3 hr during the active MJO periods (Sakaeda et al., 2017). Indeed, over the maritime continent, much of the MJO precipitation is diurnally varying precipitation (Peatman et al., 2014). Motivated by the paucity of in situ data within the MJO initiation region in the central IO, the Cooperative Indian Ocean Experiment in the Year 2011/Dynamics of the MJO field campaign was conducted from September 2011 to March 2012 (CINDY/DYNAMO, henceforth referred to as DYNAMO). The most extensive observations were taken during October–December 2011. These data provide a unique opportunity for comparison with satellite-based estimates of the diurnal cycle. The field campaign sampled a sequence of suppressed periods and eastward propagating MJO convective envelopes (Yoneyama et al., 2013). One topic of active research is how the nature of convection and the diurnal cycle of convection varies between the active and suppressed periods. Ruppert and Johnson (2015) focused on the preonset suppressed periods of the October 2011 (MJO1) and November 2011 (MJO2) events. They found a strong afternoon maximum of convection during those suppressed periods, which they viewed as a contributing factor for moisture build up leading to the active phase. In these suppressed periods with relatively calm winds, the top few meters of the sea can warm by up to 0.8°C in the afternoon, which is associated with enhanced air-sea latent and sensible heat fluxes (Matthews et al., 2014; Sakaeda et al., 2018).

One aspect of diurnal variability in precipitation not fully addressed by the above previous studies is how the life cycle of organized mesoscale cloud systems may be influenced by the MJO and how this affects the diurnal cycle of precipitation (CH97). In this study we track convective cloud systems through their life cycle. This

approach allows us to fully examine the size and lifetime of large, long-lasting convective systems that contribute to the night-morning rain and cold cloud maxima as well as short-lived small systems that contribute to the secondary afternoon maxima. Cloud fraction and rain type (e.g., shallow/deep and convective/stratiform) as used in previous studies cannot address directly the convective system lifecycle in relation to the diurnal cycle. In addition to the MJO in the equatorial region, DYNAMO shipborne and moored data also cover the ITCZ south of the equator. This study investigates the diurnal cycle of precipitation and corresponding surface forcing (e.g., SST and winds) in the ITCZ and the MJO in context of the distinct large-scale dynamic regimes of the active MJO, suppressed MJO, and the ITCZ.

The remainder of this article is organized as follows. Section 2 presents the data and methods used in this study. The seasonal mean climatology of rain and DYNAMO seasonal rain is discussed in section 3. Section 4 focuses on the air-sea forcing of afternoon convection during DYNAMO. Section 5 presents the TMPA depiction of the central equatorial IO diurnal cycle of rain. Finally, the diurnal evolution of cloud clusters and tracked time clusters is presented in section 6. Conclusions are given in section 7.

2. Data and Methods

2.1. DYNAMO Data

The DYNAMO field campaign was conducted over the central IO during September 2011 to March 2012. This study focuses on October–December 2011 when the most extensive observations were taken. The main DYNAMO data sets used in this study are radar and ship data. Four radars are used. The S-PolKa: S-band/Ka-band Dual Polarization, Dual Wavelength Doppler Radar (Lutz et al., 1995; UCAR/NCAR-Earth Observing Laboratory, 1996) was located on Addu Atoll in the Maldives, along with the 5-cm Shared Mobile Atmospheric Research and Teaching Radar (SMART-R). S-PolKa operated simultaneously at 10 cm (S band) and 0.86 cm (K_a band) wavelengths, but only the S-band data are used in this study. While SMART-R and S-Polka were located within a few miles of each other on Addu Atoll, they operated at different frequencies and were processed independently. Furthermore, SMART-R did not sample a ~20° azimuth wedge to the northwest due to beam blockage by the truck it was mounted on, and the S-PolKa beam was attenuated by the terrain on the west side at low elevation angles (e.g., 2.5°). While SMART-R reflectivities were adjusted using S-PolKa and TRMM, differences in estimated rain rates from C-band and S-band radars are still expected. Note that quantitative radar rain estimation is not a focus of this study, which is focused on the diurnal cycle.

Meanwhile, the National Aeronautics and Space Administration (NASA) TOGA (Tropical Ocean – Global Atmosphere) C-Band radar was on board the R/V *Roger Revelle*, (hereafter *Revelle*), and the R/V *Mirai* (hereafter *Mirai*) had an onboard C band radar, referred to as the *Mirai* radar. The TOGA radar is a modified Weather Surveillance Radar (WSR)-74, which was first used in TOGA-COARE (TOGA - Coupled Ocean Atmosphere Response Experiment). For each radar, volume scans were taken with coverage out to 150-km radius. For the S-PolKa radar, the volume scans were every 15 min, and for the SMART-R and the ship radars they were every 10 min. The radar data have been processed and gridded to a 1-km Cartesian grid in a consistent manner as part of the DYNAMO Legacy Data collection (see Acknowledgments section for the access link). For details regarding the radar processing, see Powell and Houze (2013) and Zuluaga and Houze (2013). Ship radar data were only considered for times when the ship was within 150 km of the on-station location (Figure 1).

Shipboard radiation, surface wind, temperature data, SST, and upperocean near surface temperature data from the *Revelle* and the *Mirai* are also used in this study. For the *Revelle*, air temperature was measured by the calibrated PSD (Physical Sciences Division) and UConn aspirated air temperature sensor on the bow mast, which was the temperature sensor least affected by solar heating. Solar radiation was measured by the ship's pyrometer at the top of the forward mast. Wind speed was measured by the sonic anemometer on the bow mast, and the COARE3 algorithm was used to obtain 10-m winds. Ocean temperature was measured by the sea snake (~5-cm depth) with a warm layer adjustment, and SST was determined using a cool skin correction. For the *Mirai*, wind speed was measured at 25 m, air temperature at 21 m, and radiation at 13 m. Winds were adjusted to 10 m using the COARE 3.0 algorithm. Ocean intake temperature was at 5-m depth. Ship data were only used for the times when the ship was within 150 km of the on-station location (see Figure 1).

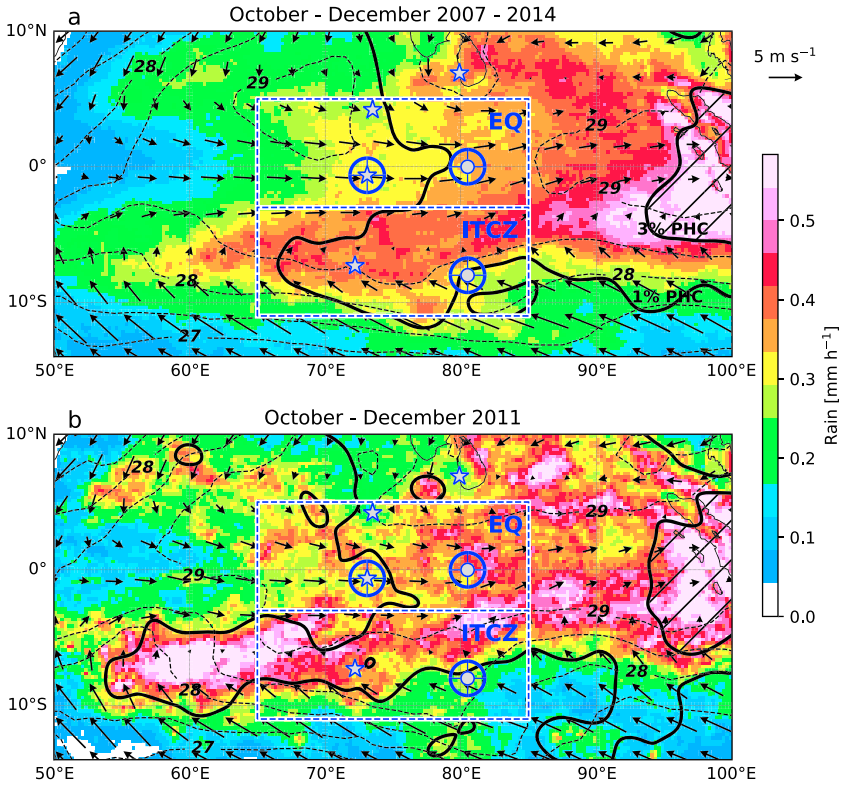

Figure 1. TMPA October to December 2007–2014 mean rain rate (color shading), mean surface winds (vectors with scale at the upper right), and infrared 208-K percent high cloud (1% and 3% contours, hatched above 3%). An 80-km Gaussian smoother has been applied to the 208 K PHC. Mean sea surface temperature is indicated by dashed black contours (every 0.5 °C). The Indian Ocean equatorial and Intertropical Convergence Zone region boxes are indicated by the dashed blue and white lines. The location of island stations (Gan, Diego Garcia, Male, and Colombo) is marked with stars and ship on station locations by circles. Radar range is drawn in blue for each site with radar data.

Rain gauges were located at Gan, Diego Garcia, on moorings, and on the ships. However, due to the nature of point rain measurements and the fact that rainfall during DYNAMO was intermittent with many nonraining days observed by the gauges, rain gauge data should be used with caution and may not be representative of the open ocean diurnal cycle. The rain gauges at the *Revelle* (*Mirai)* measured rain >1 mm/hr on 27 (17) days, respectively, and the diurnal cycle using these measurements did not corroborate well with what the onboard radars saw (not shown). While the radars do not directly measure rain, they cover a much larger representative area.

During DYNAMO, radiosondes were deployed every 3–6 hr from the island stations Gan, Male, Diego Garcia, and Colombo and from the *Revelle* and *Mirai*. Gan, Male, Colombo, and the Revelle constitute the Northern Sounding Array, which is most representative of the equatorial region (Figure 1). A procedure using European Centre for Medium-Range Weather Forecasts (ECMWF) analysis winds to mitigate the island heating and blocking effects of Sri Lanka has been carried out for the Colombo soundings (Ciesielski et al., 2014). Meanwhile, Gan, Diego Garcia, the *Revelle*, and the *Mirai* encompass the Southern Sounding Array, which straddles the ITCZ. For this study, the merged sounding/ECMWF reanalysis product is used. The product is part of the DYNAMO Legacy Data Collection. For more details on the quality control and data processing of the DYNAMO sounding products, see Ciesielski et al. (2014) and Johnson et al. (2015).

2.2. Satellite Data

2.2.1. TRMM Multisatellite Precipitation Analysis

The TMPA provides 3-hourly estimates of instantaneous rain rates on a regular 0.25° grid (TRMM, 2011). The rain rate estimates are based on passive-microwave retrievals of rain rate from TRMM TMI, AMSR-E (Advanced Microwave Scanning Radiometer for Earth Observing System), SSMI (Special Sensor Microwave Imager), and

Table 1
Classification Thresholds of Cloud Clusters and Sample Counts of Cloud Clusters and Time Clusters Occurring Within the Equatorial and Intertropical Convergence Zone Regions for October to December 2007–2014

Class	Area (km^2)	Size (km)	Cloud cluster count		Time cluster count	
Class 1	<3,518	<59	296,256	298,588	7,962[a]	8,122[a]
Class 2	3,518–14,863	59–122	12,308	12,999	4,167	4,026
Class 3	14,863–45,559	122–213	3,092	3,983	573	619
Class 4	>45,559	>213	890	1,226	128	172

[a]The time cluster counts for the class 1 clusters are for a minimum area of 100 km^2.

AMSU (Advanced Microwave Sounding Unit). When passive microwave data are not available (e.g., ~10% of the time during the study period), infrared-based rain estimated are used. See Huffman et al. (2007) for further details regarding the TMPA. The October–December seasonal mean rainfall for 2007–2014 and for 2011 (DYNAMO) is shown in Figure 1. The TMPA data provide passive microwave only rainfall estimates and merged rainfall estimates using IR derived rainfall when there is no passive microwave data. For Figure 1, the merged product is used, but for documenting the diurnal cycle only the microwave estimates are used (TMPA MW). In order to explore the diurnal cycle beyond DYNAMO, TRMM data and IR data are used for the 8-year overlapping Meteosat 7 Indian Ocean data coverage period and TRMM period: October to December 2007–2014. For this analysis, the TMPA MW was used instead of the merged TMPA to ensure independence between the rain and IR data.

2.2.2. Infrared Satellite Data

The National Oceanic and Atmospheric Administration/Climate Prediction Center maintain a half-hourly IR data set at 4-km resolution from 60°S to 60°N (Janowiak et al., 2001). The data are archived at NASA as a TRMM/GPM (Global Precipitation Measurement) supporting data set. This study uses hourly data on the half hour, which have more consistent complete coverage in the IO and west Pacific Ocean. IO data coverage has been provided by Meteosat 7 since 2006. Meteosat 7 is last of the first generation Meteosat series satellites. During the study period, it was positioned over the equator at 57.8°E. Its infrared channel is centered at a wavelength of 10.5–12.5 μm. Meanwhile, over the western Pacific Ocean, MTSAT1R provided data through June 2005, and MTSAT2 provided data starting in 2010 through July 2015. The MTSAT (Multi-functional Transport Satellite) series satellites were located at the equator and 140°E. MTSAT uses the IR channel of 10.3–11.3 μm. (Note that during TOGA-COARE, western Pacific coverage was provided by GMS4 with the IR sensor centered at 10.5 μm, and calibration differences may exist between GMS and Meteosat7).

The global merged data set is created as follows. The IR data from the GOES (Geostationary Operational Environmental Satellite), GMS, MTSAT, and Meteosat have been geomapped to a regular 0.0364° (~4 km at the Equator) latitude-longitude grid from 60°S to 60°N using the Man computer Interactive Data Access System (a.k.a. McIDAS). For the overlapping regions, the MTSAT data were used, since it is a second generation satellite. Zenith angle corrections are applied to correct so-called *limb darkening*, resulting in warmer temperatures at the periphery of the satellite view compared with not accounting for zenith angle. However, satellite intercalibration was not done, resulting in a discontinuity at the eastern edge of the Meteosat data used, near 87°E (not shown). The analysis of IR satellite data is from 65°E to 85°E in order to avoid any effects from this discontinuity. In order to ensure the consistency of the satellite data over the central IO, the study period is limited to October–December 2007–2014, which is within the overlapping Meteosat 7 and TRMM era.

Using the merged 4-km IR data, percent high cloud (PHC) was calculated for the 208K threshold (208-K PHC). The hourly diurnal 208-K PHC is the percentage of all grid points within the EQ or ITCZ box for each local time bin (0–1 LT, etc.). The IR data were also used for cloud cluster tracking, following CH97. Using the hourly merged 4-km infrared satellite data, cloud clusters were identified as contiguous areas with brightness temperatures below 208 K. Diagonal connectivity was not allowed. The size distribution was determined based on the cumulative area contribution using 100-km^2 area bins. The four quartiles are denoted class 1, class 2, class 3, and class 4 (Table 1). Due to different IR bands and satellite calibrations, the cloud cluster size distribution differs from Chen et al. (1996) and CH97. The cloud clusters are tracked in time as time clusters when they overlap with preceding/succeeding cloud clusters by the smaller of 50% of the area of 5,000 km^2. Cloud

clusters involved in mergers, and splits are retained together as part of the same time cluster. The maximum areal extent of the time cluster throughout its lifetime is used to determine its class, using the same thresholds as cloud clusters.

In this study, a *bootstrap* statistical test is used to determine the statistical significance associated with the diurnal cycle of cloud cluster initiation, maximum areal extent, and dissipation as well as cloud cluster duration. Bootstrap analysis is advantageous because it does not make assumptions about the form or shape of the data distribution. Independent bootstrap tests were carried out for each class of cloud clusters. This was done for EQ and ITCZ independently. The 95% confidence interval was determined by randomly resampling the clusters with replacement and recalculating the diurnal cycle and the duration histogram. One thousand bootstrap instances were used.

2.2.3. CCMP Surface Winds

To document the surface wind patterns and convergence/divergence in relation to the satellite rainfall and cold clouds, the Remote Sensing Systems Cross-calibrated Multiplatform (CCMP) surface wind velocity dataset is used (Wentz et al., 2015). The CCMP provides instantaneous winds every 6 hr at quarter-degree spatial resolution (Atlas et al., 2011). The CCMP uses ECMWF Interim Reanalysis as a background first guess and incorporates wind estimates from AMSR-E, AMSR2, TMI, GMI, QuikSCAT, ASCAT (Advanced Scatterometer), SSMI (Special Sensor Microwave Imager), SSMIS (Special Sensor Microwave Imager/Sounder), and Windsat. It also incorporates moored buoy wind data. This data set goes back to 1987 and is geared toward climate studies including air-sea fluxes.

2.3. Diurnal Cycle Frequency Distribution of Rain Rate

To quantify the diurnal cycle, the radar and satellite TMPA rain data were binned into logarithmic rain rate bins and hourly (3-hourly) local time bins for radar (satellite) data. The rain rate bins were every 5 dB or rain rate, specifically: 0.1, 0.3, 1.0, 3.2, 10.0, 32.0, 100, and $>$100 mm/hr. For the 10- to 15-min resolution radar data, hourly local time bins were used, and for the 3-hourly satellite data 3-hr bins were used. To construct the diurnal frequency distribution of rain rates, the total count of occurrences in each rain rate bin over the diurnal cycle was determined, and each of the counts for individual local time bins within that rain rate bin were normalized by the total rain rate bin count. The frequency distribution is expressed as a percent occurrence for each rain rate/hour bin. However, rain rate bins with fewer than 100 samples across the diurnal cycle were not considered. This technique is analogous to the contoured frequency by altitude diagram technique commonly used to compare the vertical profiles of deep convection (Yuter & Houze, 1995). It is chosen to better highlight the diurnal cycle of the heavier rain rates ($>$10 mm/hr), which are much less frequent than the lighter rain rates.

Note that the TMPA rain rates are smaller than the radar rain rates since they represent a 0.25° by 0.25° area. For the radar rain rates at 1-km resolution, rain rates smaller than 1 mm/hr are not considered, but for TMPA rain rates down to 0.1 mm/hr are considered. Nevertheless, TMPA data for the 0.1–1.0 mm/hr bins should be interpreted with caution.

2.4. Association Between TMPA Rain and Cloud Clusters

There are two challenges with associating cloud clusters with the satellite estimated rain. The first is spatial resolution. The TMPA quarter-degree grid represents ~700 km^2 near the equator. Many class 1 cloud clusters are smaller than the TMPA data grid cells. In fact, two or more class 1 clusters are often present within a single TMPA grid cell. Furthermore, the larger cloud clusters partially overlap with the TMPA grid cells along their perimeters. To partially alleviate this area mismatch, the mean rain rate of the TMPA grid cells that overlap with the cloud cluster was taken and multiplied by the cloud cluster area to obtain a volumetric rain rate. The TMPA data contain the timing of the satellite data (e.g., microwave swath or infrared image) used for each grid cell rain estimate, and the TMPA cell that was closest in time to the cloud cluster time is used. The volumetric rain rate is used to determine the contribution to the overall equatorial region or ITCZ box rain rate (in mm/hr) by dividing by the area of the box. Because the local rain rate of class 1 clusters is likely greater than the 0.25° averaged rain rate, this likely underestimates the rain contribution of small systems. Furthermore, rain that is physically connected with the same cloud system may occur outside of the 208-K contour. Thus, the overall contribution of the 208-K cloud systems to the total rainfall is likely underestimated in this study. It is anticipated that using the GPM IMERG (Integrated Multi-satellitE Retrievals for GPM) data set,

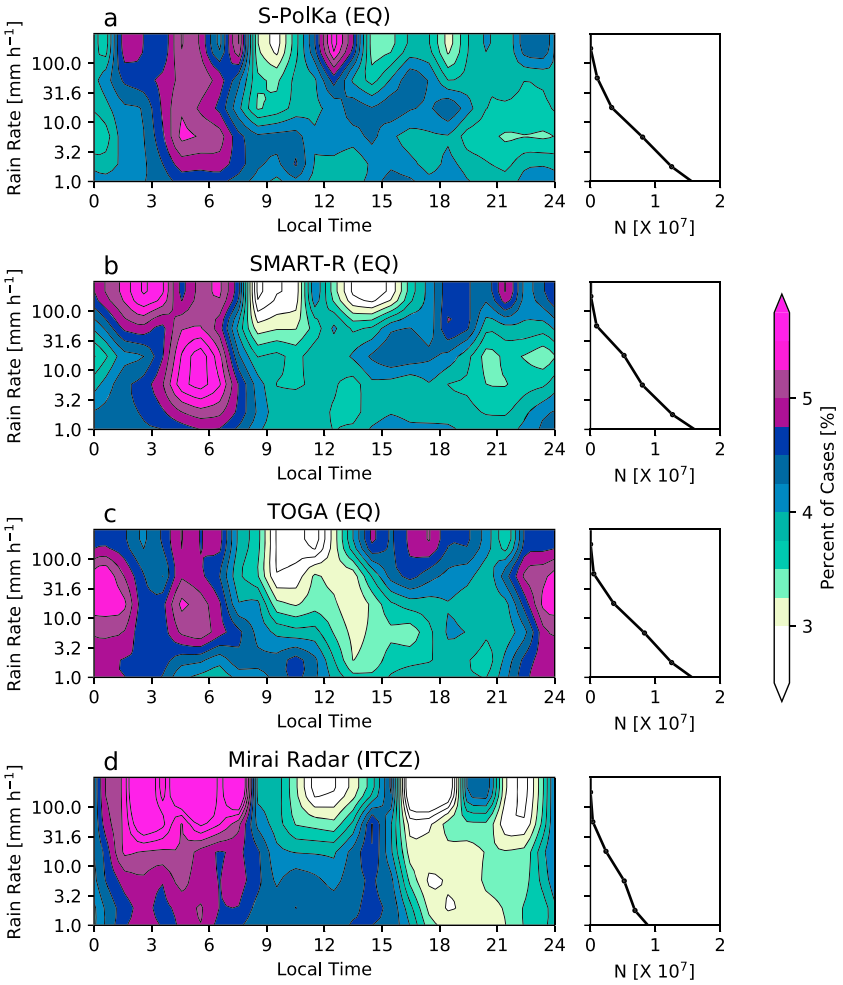

Figure 2. Diurnal cycle frequency distribution of rain rates from the (a) SMART-R, (b) S-PolKa, (c) TOGA, and (d) R/V *Mirai* radar. The color shading indicates the percentage of samples within each bin, normalized by the number of samples in each rain rate bin. Local time bins are hourly and rain bin edges are indicated by the ticks on the *y* axis. The number of samples within each rain rate bin is shown on the right side. EQ = equatorial; ITCZ = Intertropical Convergence Zone.

which is at 0.1°, half-hourly resolution, could help alleviate these issues; however, as of the writing of this paper, that data are only available for the GPM era, which is after the period of this study.

3. Seasonal Rain and Cold Clouds

The October–December seasonal rainfall is greatest in the eastern Indian Ocean and in the Southern Hemisphere ITCZ (Figure 1a). Seasonal mean rainfall of >0.6 mm/hr occurs just offshore of Sumatra, with a gradual decrease in rainfall from east to west. In the central IO, the Southern Hemisphere ITCZ is roughly defined by rainfall >0.4 mm/hr at around 5–10°S. Since rainfall in the study region is predominantly produced by deep convection, the areas of heaviest rain are generally associated with greater cold cloud (208 K) coverage (Figure 1a). A secondary rainfall maximum occurs in the eastern IO to the east of Sri Lanka. The equatorial region is chosen to represent the equatorial rainfall minimum with respect to latitude over the central IO and to avoid land influence from southern India and Sri Lanka.

The DYNAMO observation array spanned the equatorial region, the ITCZ, and the Southern Hemisphere trade wind regions (Chen et al., 2016; Yoneyama et al., 2013). Gan (0.63°S, 73.1°E) and the *Revelle* (stationed near 0°N, 80.5°E) were located within the equatorial region. During DYNAMO the rainfall minimum (with respect to latitude) over the central equatorial IO was less pronounced than the climatology (Figure 1). This is a

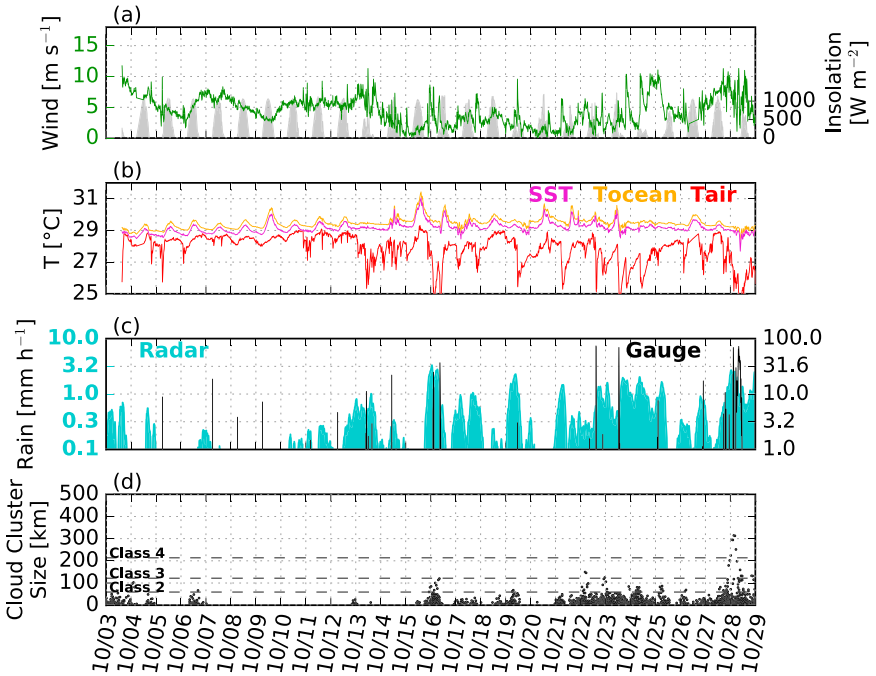

Figure 3. Time series of (a) wind speed (green) and insolation (gray); (b) sea surface temperature (SST; magenta), upper ocean temperature (orange) and air temperature (red), (c) rain gauge (black) and 150-km radius radar rain rates (cyan), and (d) cloud cluster size (square root of the area) for the R/V *Revelle* during 3–28 October 2011.

reflection of the particularly active MJO season that year (Gottschalck et al., 2013). Diego Garcia (7.3°S, 73.4°E) was located in the ITCZ but unfortunately did not have a radar installed. The ITCZ extended further west during DYNAMO than in the 2007–2014 mean, and it was less distinct from the EQ region in the central IO (Figure 1b). In contrast, the *Mirai* (stationed near 8°S, 80.5°E) was at the southern edge of the

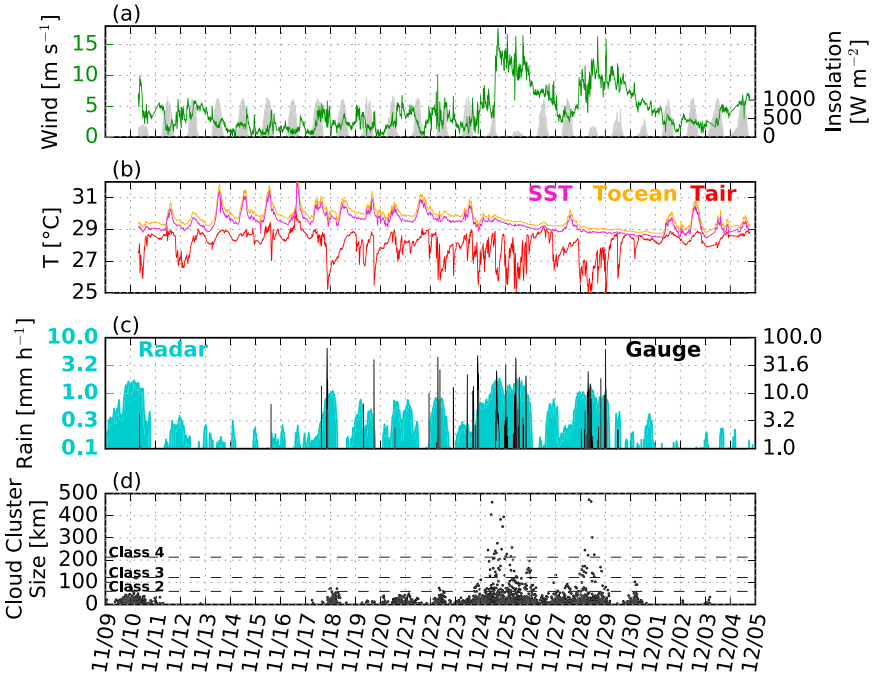

Figure 4. Same as Figure 3 but for the R/V *Revelle* during 9 November to 4 December 2011. SST = sea surface temperature.

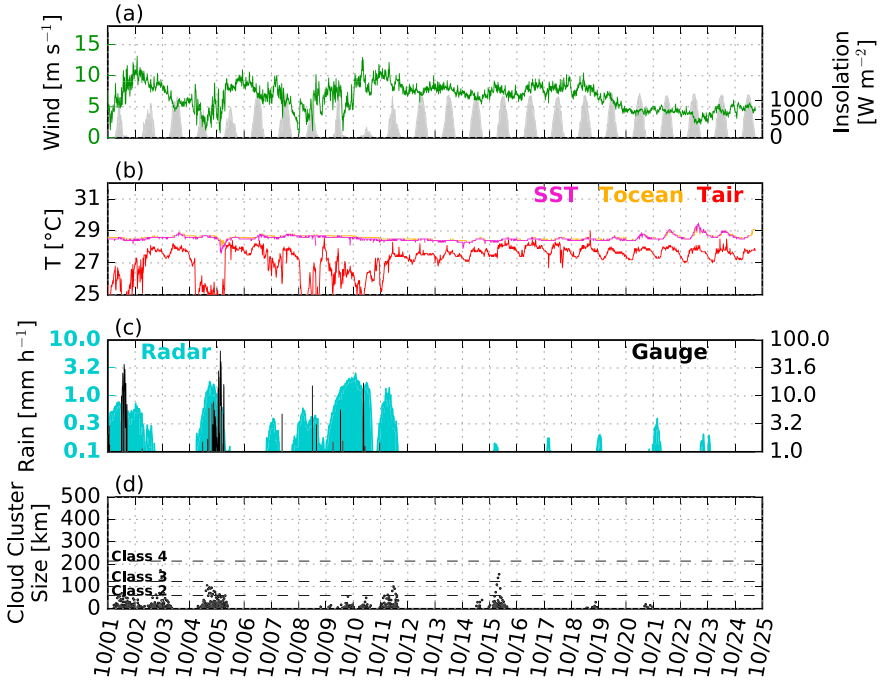

Figure 5. Same as Figure 3 but for the R/V *Mirai* during 1–25 October 2011. SST = sea surface temperature.

climatological ITCZ but southeast of the main ITCZ convection during DYNAMO (Figure 1). The conditions experienced by the *Mirai* were more typical of the trade winds than the heart of the ITCZ (Yokoi et al., 2014). Meanders of the ITCZ occasionally affected the *Mirai*, and the ship radar was able to sample ITCZ convection, especially to the north.

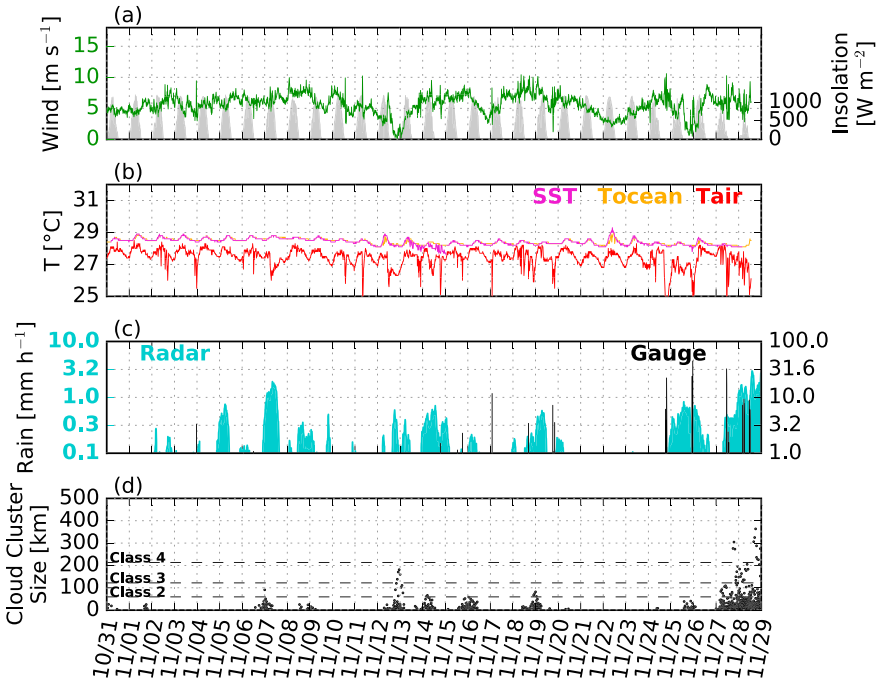

Figure 6. Same as Figure 3 but for the R/V *Mirai* during 31 October to 29 November 2011. SST = sea surface temperature.

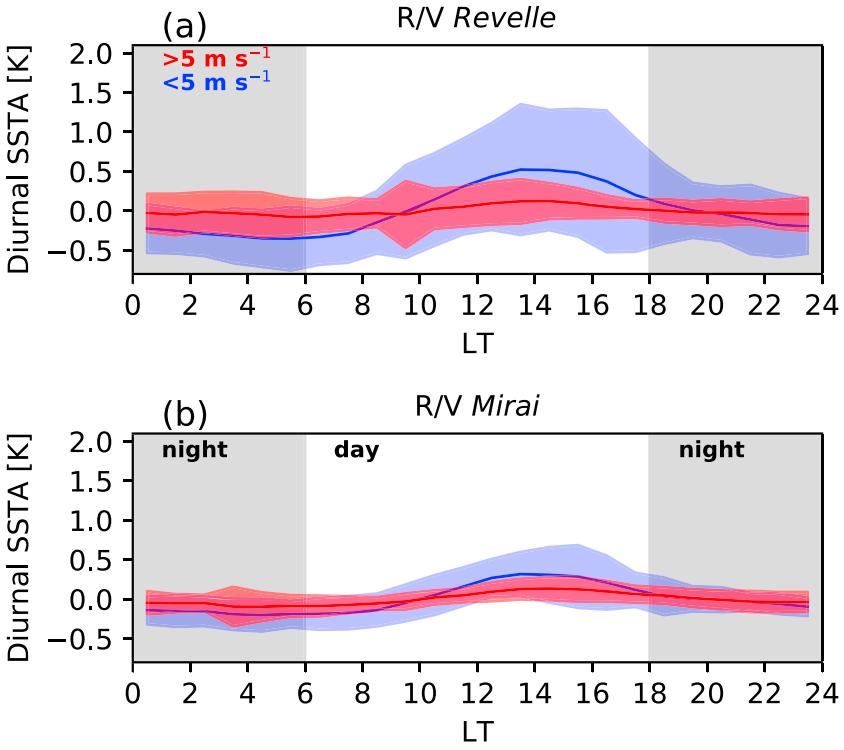

Figure 7. Diurnal cycle of sea surface temperature anomaly from the daily mean for (a) the *Revelle* and (b) the *Mirai*. Red (blue) curves are for days with daily mean wind speed greater than (less than) 5 m/s. The hourly mean is drawn as a curve, and the shaded areas are for two standard deviations below and above the mean.

4. Diurnal Cycle and Air-Sea Forcing During DYNAMO

4.1. Early Morning Rain Maximum

The most extensive surface rain rate data during DYNAMO was derived from the radars. As expected, the radar estimated rain has a dominant diurnal maximum in the morning. For the S-PolKa radar and SMART-R

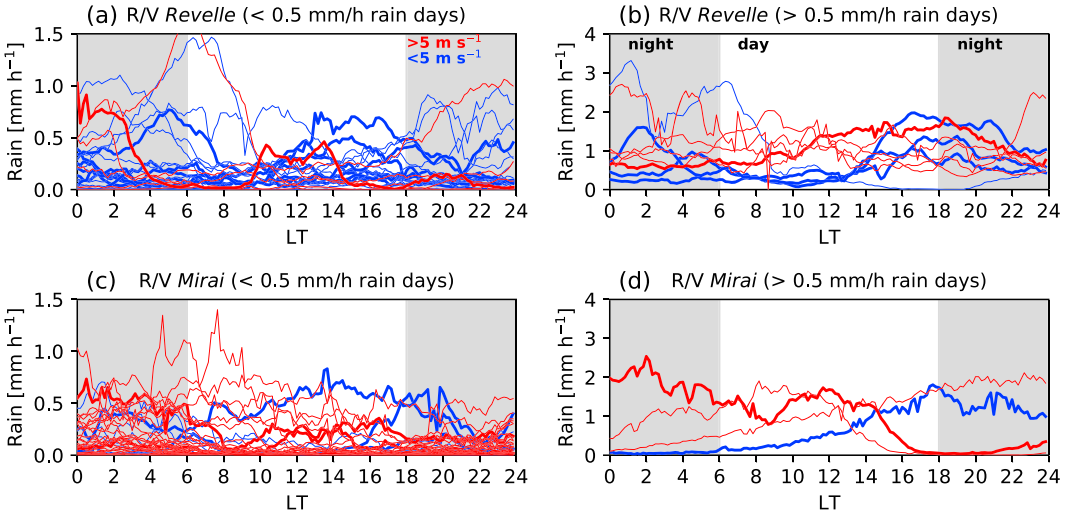

Figure 8. Diurnal cycle of radar average rain rate: (a) days with <0.5 mm/hr daily mean rain at the *Revelle*; (b) days with >0.5 mm/hr daily mean rain at the *Revelle*; (c) days with <0.5 mm/hr daily mean rain at the *Mirai*, and d days with >0.5 mm/hr daily mean at the *Mirai*. Red (blue) curves are for days with daily mean wind speed greater than (less than) 5 m/s. Days with an afternoon radar rain maximum are drawn thick.

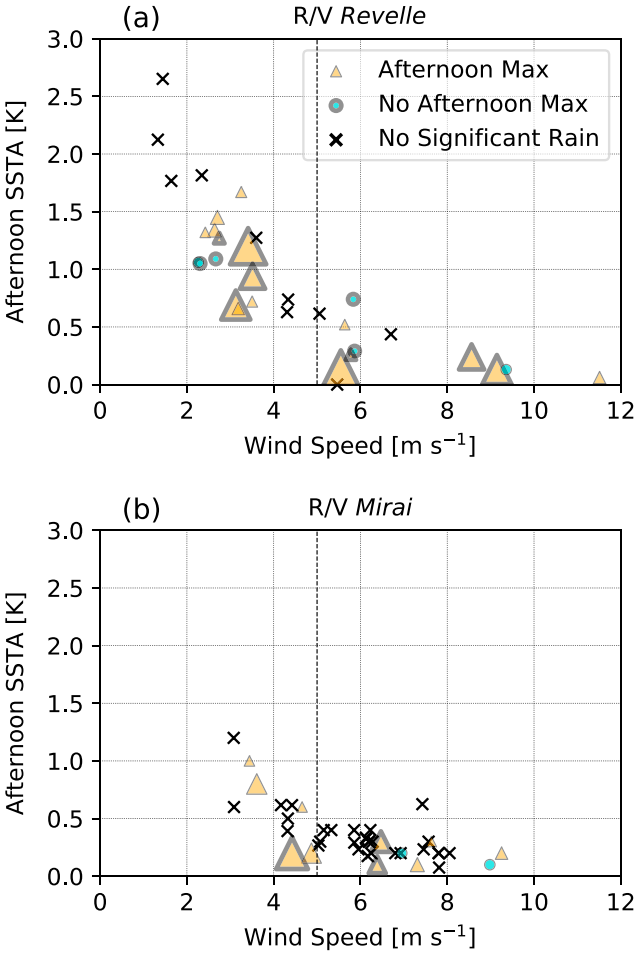

Figure 9. Scatter plot of daily mean wind speed and afternoon maximum sea surface temperature anomaly (SSTA) from the 4–6 LT mean SST for (a) the R/V *Revelle* and (b the R/V *Mirai*. Orange triangles are for days with an afternoon radar rain maximum. The size of the triangle is proportional to the amplitude of the afternoon maximum (see text for details). Cyan circles are days with afternoon rain >0.1 mm/hr but no afternoon maximum. X markers are for days with afternoon rain <0.1 mm/hr. Markers are drawn with a thick border for days with daily mean radar rain >0.5 mm/hr.

on Addu Atoll, the morning maximum is from 0100 to 0800 LT and midnight—0800 LT, respectively (Figures 2a and 2b). The morning maximum begins a few hours earlier for rain rates >32 mm/hr. The TOGA radar has the nocturnal maximum beginning somewhat earlier—at around 2200 LT (Figure 2c). Finally, for the *Mirai* radar, the nocturnal maximum is from midnight to 0800 LT.

4.2. Secondary Afternoon Rain Maximum

The radar data reveal regional significant differences in the diurnal cycle of rainfall, especially for heavier rain rates in the afternoon and evening. The diurnal cycle frequency distribution of rain rates is used to highlight the afternoon peak. For each of the radars, the nocturnal maximum (midnight—0600 LT) is the dominant feature of the diurnal cycle (Figure 2). Additionally, each of the radars had a relative minimum rain occurrence from 0900 to 1200 LT. However, during the afternoon and evening the diurnal cycle differs markedly between the equatorial region radars (S-PolKa, SMART-R, and TOGA) and the *Mirai* radar, which sampled the ITCZ.

The S-PolKa radar has a secondary maximum in the occurrence of 3–32 mm/hr rain rates from 1200 LT to 1800 LT (Figure 2a). The SMART-R radar diurnal cycle is similar to the S-PolKa except for the timing of peaks for rain rates >100 mm/hr, of which there are few samples (Figure 2b). These differences between SMART-R and S-Polka are due to a combination of sampling, frequency bands, and processing as discussed in section 2.1. For the TOGA radar, the afternoon maximum is reflected in rain rates >10 mm/hr for 1400–2000 LT (Figure 2c). While the *Mirai* radar data have an afternoon maximum around 1400 LT, it was mainly contributed by the strong mesoscale convective system on 28–29 November (Judt & Chen, 2014). Instead, the distinctive feature of the diurnal cycle as seen by the *Mirai* radar is the distinct minimum from 1600 to 2200 LT (Figure 2d). The diurnal cycle difference between the S-PolKa, SMART-R, and TOGA radars in the equatorial region and the *Mirai* radar, which sampled the ITCZ, was in the afternoon into the evening. The TOGA radar had the most pronounced secondary afternoon maximum.

4.3. Air-Sea Forcing and Convection During DYNAMO

Previous work has shown that the diurnal cycle of SST over the open ocean can be substantial, up so several degrees Celsius (Chen & Houze, 1997; Li et al., 2013; Lukas & Lindstrom, 1991; Matthews et al., 2014; Sakaeda et al., 2018). The afternoon elevation of the SST can trigger an afternoon maximum in rain or afternoon rain which grows into the night contributing to the nocturnal maximum. As discussed above, the TOGA radar observed a secondary maximum most pronounced for rain rates >10 mm/hr, which was not the case for the *Mirai* radar (Figure 2). The *Revelle* and *Mirai* ship surface data depict how the air-sea forcing leads to different preferred diurnal cycle regimes between the two locations.

4.3.1. Light Wind Regime

Diurnal air-sea forcing is a byproduct of day time insolation that exceeds 1,000 W/m^2 most days (Figures 3a, 4a, 5a, and 6a). Whether the SST has a significant afternoon maximum depends on how deep the heating is distributed through the upper ocean, which is a function of upper ocean mixing. Upper ocean mixing depends on wind speed and ocean stratification, of which wind speed is the dominant factor in the tropical ocean. During DYNAMO, days with wind speeds below 5 m/s had afternoon SST maxima of up to several degrees Celsius higher than the early morning, for example, 14–23 October and 10–23 November at the *Revelle* (Figures 3a, 3b, 4a, and 4b) and 20–24 October at the *Mirai* (Figures 5a and 5b). At the *Revelle* these low wind periods with strong SST maxima occurred in stretches of several weeks, which is the suppressed MJO. Many of these days had little to no rainfall and 208-K cloud clusters, such as

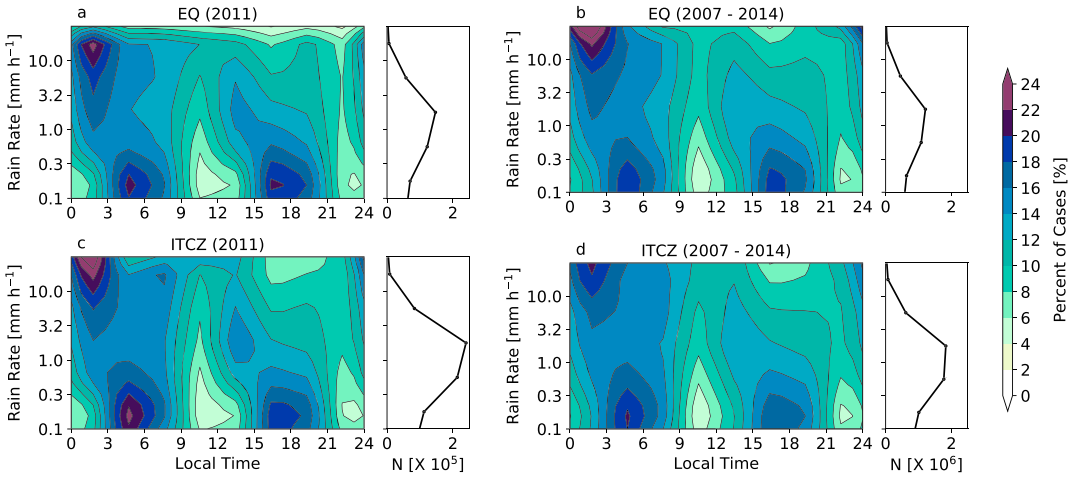

Figure 10. Diurnal cycle frequency distribution of rain rate from Tropical Rainfall Measurement Mission Multisatellite Precipitation Analysis MW. (a) Equatorial (EQ) region for October–December 2011, (b) EQ region for October–December 2007–2014, (c) Intertropical Convergence Zone (ITCZ) region for October–December 2011, and (d) ITCZ region for October–December 2007–2014. The color shading is for the percentage of samples within each bin, normalized by the number of samples in each rain rate bin. Local time bins are 3-hourly and rain bin edges are indicated by the ticks on the *y* axis. The number of samples within each rain rate bin is shown on the right side.

13–16 November (Figures 4c and 4d). In contrast, at the *Mirai* light winds with a strong afternoon SST maximum was an intermittent occurrence. For both the *Revelle* and *Mirai*, the days with wind speed $<$5 m/s had much more diurnal SST warming compared with the days with higher wind speeds (Figure 7). The SST warming tended to be more pronounced at the *Revelle* than the *Mirai* for the days with wind speed $<$5 m/s, which is likely due to lighter wind speeds at the *Revelle* compared with the *Mirai* during the $<$5 m/s periods.

4.3.2. Moderate to High Wind Regime

On days with winds $>$5 m/s, the afternoon warming of the SST was a few tenths of a degree or nonexistent (Figure 7). At the *Revelle*, this mainly occurred during the active periods of the MJO (Figure 7a): MJO1 and MJO2 as denoted by Gottschalck et al. (2013). During DYNAMO, insolation was significantly reduced only during a few active MJO days with widespread convection and large cloud clusters, such as 24–25 October 2011 and 28–30 November 2011 at the *Revelle* (Figures 3 and 4). For the *Mirai*, active convection days with reduced insolation, elevated wind speeds, and weak SST maxima occurred on 9–11 October and 27–28 November (Figures 5 and 6). It is not surprising that there was a weak diurnal cycle of SST on those days (Figure 7b). During the active MJO periods with strong winds $>$10 m/s nocturnal maxima without subsequent afternoon sometimes occurred (e.g., Figure 8).

Not surprisingly, the afternoon SST maxima observed by the *Mirai* were much weaker than at the *Revelle*, although there were some days with afternoon SST 0.5–1 °C higher than the early morning when the winds fell below 5 m/s (Figure 7b). Unlike at the *Revelle*, at the *Mirai* winds $>$5 m/s generally occurred together with strong insolation. The daytime solar forcing was not able to overcome the upper ocean mixing and significantly (e.g., $>$0.5 °C) warm the sea surface in this regime. The next section explores in more detail the SST and wind conditions, which are associated with an afternoon rain maximum.

4.4. Afternoon Rain Maxima, Wind Speed, and SST

While there were many days with low winds and significant afternoon SST warming, for many of those days little rain occurred. Here days with $<$0.1 mm hr average rain rate from 1200 to 1800 LT within the 150-km radar range are defined as *no afternoon rain* days. The unconditional average, which includes radar data points without rain, is used. For the days with 1200–1800 LT radar rain $>$0.1 mm/hr, afternoon maxima were determined by comparing the 2-hr mean centered on the maximum rain rate for 1200–1800 LT compared with the morning average rain rate from 0800 to 1000 LT and the nighttime rain rate from 2200 to 2400 LT. These time intervals were chosen a priori to ensure that days with early morning rain maximum could still be identified as having secondary afternoon rain maxima. If the morning and afternoon rain maxima were

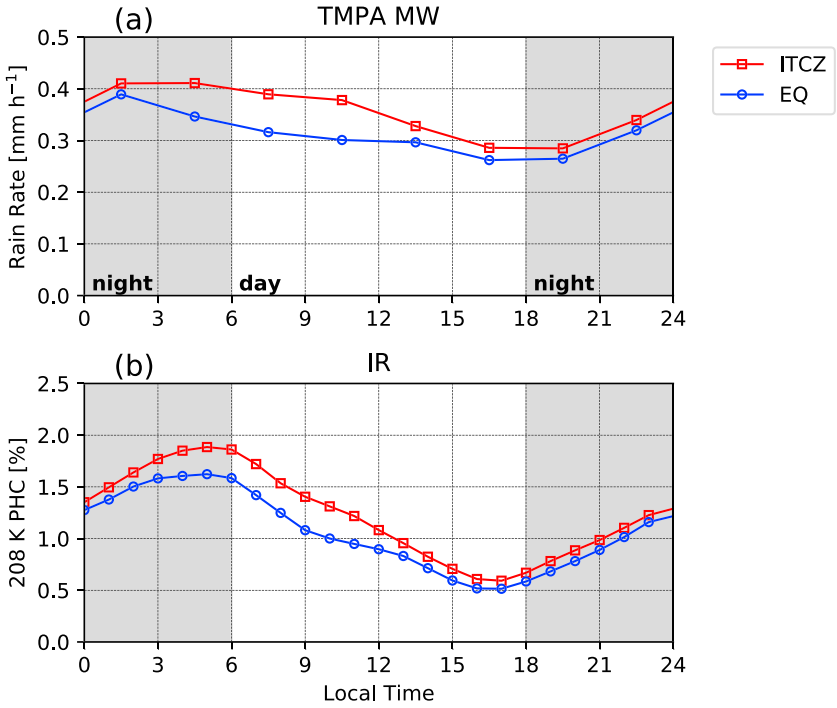

Figure 11. Diurnal cycle of a TMPA rain rate (MW only) and b PHC 208 K for October–December 2007–2014 for the ITCZ region (red) and the IO region (EQ; blue). TMPA MW = Tropical Rainfall Measurement Mission Multisatellite Precipitation Analysis microwave; PHC = percent high cloud; ITCZ = Intertropical Convergence Zone; IO = Indian Ocean.

less than 75% of the afternoon 2-hr max rain, the day is considered to have an afternoon maximum. For the *Revelle* (*Mirai*), 12 (7) days were identified with afternoon rain maxima. Sensitivity tests varying the average rain rate threshold (0.06–0.14 mm/hr) and morning/evening percentage (65%–85%) showed that while several (e.g., 1–4) marginal cases were sensitive to the criteria, the main conclusions were not affected (not shown). The rain rate difference between the 2-hr afternoon maximum and the average of the morning and nighttime minima is considered to be an indicator of how strong the afternoon maximum was that day. The days with afternoon maxima are shown in Figure 8. Most days with afternoon maxima were associated with winds $<$5 m/s during days with relatively light rainfall ($<$0.5 mm/hr averaged over the day; Figures 8a and 8c). There were relatively fewer days with daily mean rain $>$0.5 mm/hr, of which four days had afternoon maxima at the *Revelle* (Figure 8b) and two days had afternoon maxima at the *Mirai* (Figure 8d).

Figure 9 summarizes the relationship between wind speed, afternoon SST warming, and afternoon rain maxima for the *Revelle* and the *Mirai*. As discussed above, afternoon SST warming of $>$0.5 °C is generally associated with wind speeds $<$5 m/s, and those days tend to either have afternoon maxima or are suppressed with little afternoon rain. During DYNAMO, the *Revelle* experienced this regime much more often than the *Mirai*. Furthermore, days with daily mean rain rate $>$0.5 mm/hr are considered to be convectively active days. Those convectively active days account for the days with the strongest afternoon maxima as well as most of the days with afternoon maxima in the $>$5 m/s regime. One scenario unique to the *Mirai* was many days with little rain, moderate wind speeds, and afternoon SST warming $<$0.5 °C, which was not observed at the *Revelle*.

Morning rainfall occurred both on days with and without afternoon maxima. The no afternoon rain days tended to have morning maxima, consistent with the findings of Sakaeda et al. (2018). Additionally, some days with afternoon maxima also had preceding morning maxima earlier in the day. These cases may have been associated with a reinvigoration of convective rain occurring after the broad stratiform rain areas, which have a nocturnal maximum, have diminished (Zuluaga & Houze, 2013). Thus, both no afternoon rain days and days with afternoon maxima contributed to the morning rain maximum.

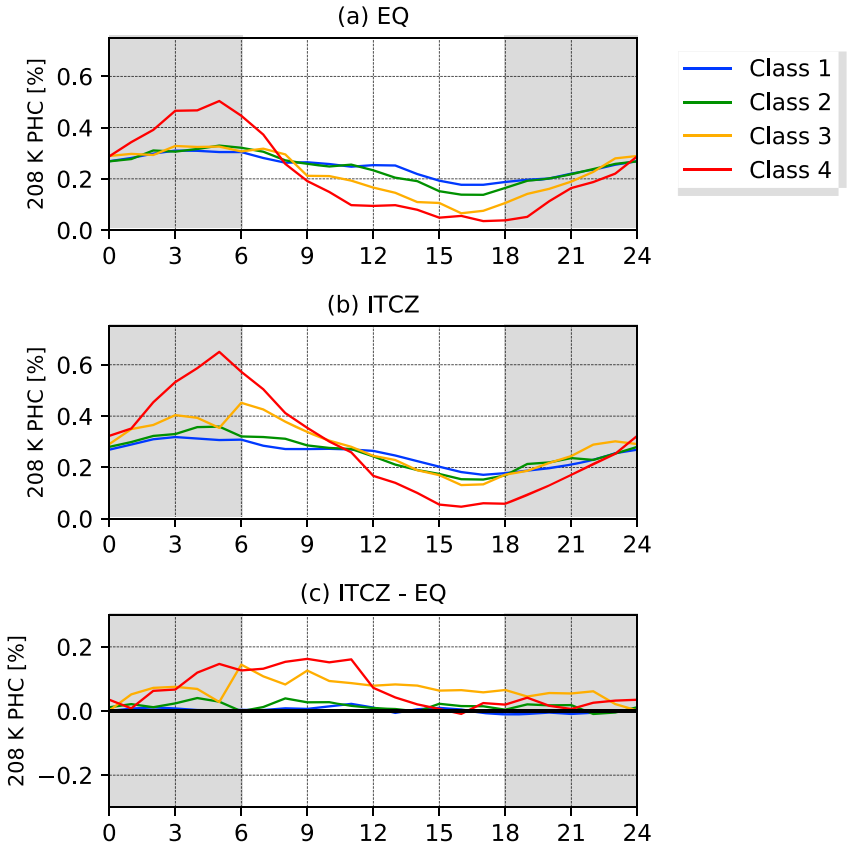

Figure 12. The diurnal cycle of the 208-K PHC area encompassed by cloud clusters of class 1 (blue), class 2 (green), class 3 (orange), and class 4 (red) within (a) the equatorial (EQ) region, (b) the ITCZ region, and (c) the ITCZ − EQ difference. The time period is to OctoberDecember 2007–2014. PHC = percent high cloud; ITCZ = Intertropical Convergence Zone.

5. Satellite and Radar Rain Rate Diurnal Cycle Comparison

The diurnal cycle of rain frequency for and the 8-year overlapping TMPA and Meteosat 7 period as seen by TMPA MW is shown in Figure 10. The DYNAMO year diurnal cycle is similar to the extended period. The diurnal cycle from TMPA MW during DYNAMO for the equatorial region and ITCZ was nearly identical to using only TMPA grids within 300 km of the *Revelle* and *Mirai*. In both the equatorial region and ITCZ, the nocturnal maximum peaks at 0000–0300 LT for rain rates >10 mm/hr, and it lasts until 0600–0900 LT for rain rates <10 mm/hr. The timing of the nocturnal maximum seen from TMPA MW differs from that seen by the radars. None of the radars had such a pronounced maximum occurrence of 10–100 mm/hr rain rates at 0000–0300 LT as in TRMM MW. Instead, the nocturnal maximum varies from 0400 to 0700 LT at Gan, 22–08 LT at the *Revelle*, and 0200–0800 LT for the *Mirai* (Figure 2). The TRMM MW did not capture the variability in the nocturnal maximum as seen by the DYNAMO radars.

Similar to the nocturnal maximum, the variability in the afternoon rainfall was not well captured by the TMPA MW. A minimum in rain occurrence for all rain rates occurs at 0900–1200 LT, then a secondary afternoon maximum. For rain rates <10 mm/hr, a secondary afternoon maximum occurs between 1200 and 1800 LT. However, the afternoon maximum for rain rates >10 mm/hr seen in the *Revelle* radar data (Figure 2c) was not captured by TMPA MW. Furthermore, an afternoon maximum for rain rates <10 mm/hr was not observed by the radars during DYNAMO. Note that Sakaeda et al. (2018) also pointed out challenges in documenting the diurnal cycle using TMPA data, especially during suppressed MJO periods. Because the TMPA data did not well capture the afternoon maximum, and because previous results show that the nocturnal maximum is associated with large cloud systems, the subsequent results focus on the nocturnal maximum. Since the largest (e.g., top quartile) cloud systems are relatively rare, the extended period is used to ensure sufficient sampling of the largest, most long-lived cloud systems.

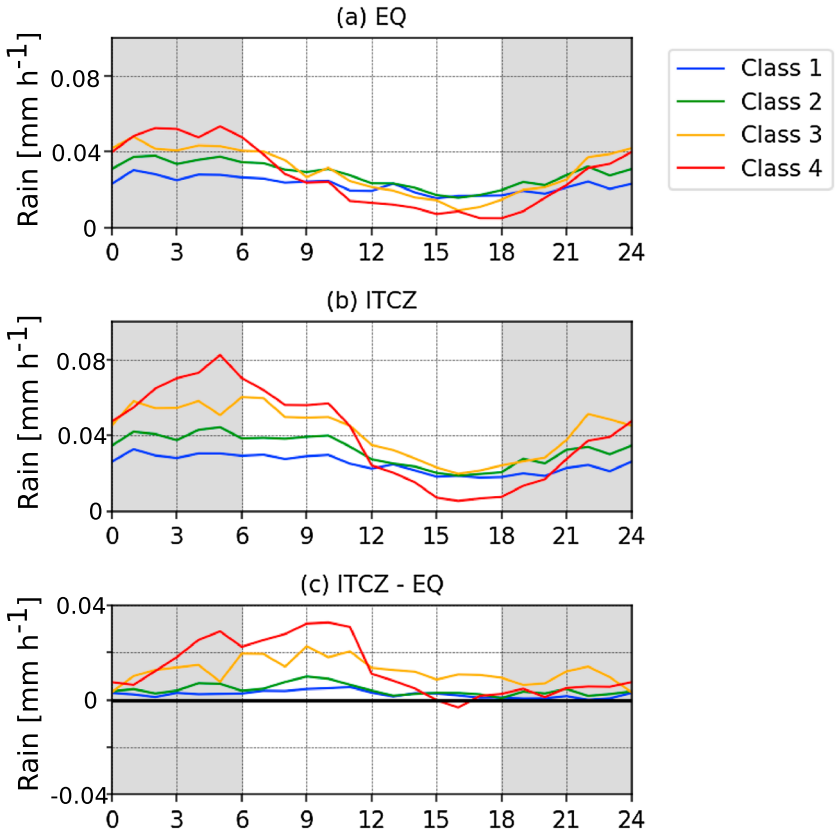

Figure 13. The diurnal cycle of the rainfall from TMPA colocated with cloud clusters of class 1 (blue), class 2 (green), class 3 (orange), and class 4 (red) cloud clusters within (a) the equatorial (EQ) region and (b) the ITCZ region. Panel (c) is the difference between the ITCZ and EQ regions. The volumetric rain is summed over each hour in October to March 2007–2015. TMPA = Tropical Rainfall Measurement Mission Multisatellite Precipitation Analysis; ITCZ = Intertropical Convergence Zone.

6. Cloud Cluster Life Cycle and the Nocturnal Maximum

6.1. Diurnal 208-K Cloudiness and Rain Contribution From Cloud Clusters

The diurnal cycles of rainfall and cold clouds were closely correlated with each other peaking between 0000 and 0600 LT, but there were differences between the equatorial region and ITCZ as well as between rainfall and cold cloud coverage. Rainfall peaked at 0000–0300 LT, while 208-K clouds peaked a few hours before sunrise at 0300–0600 LT (Figure 11). Cold clouds peak later than rainfall because they can continue to grow after the heaviest rainfall has diminished. In both the equatorial region and ITCZ, cold clouds had a distinct minimum at 1500–1800 LT, while rainfall had a broader minimum between 1500 and 2100 LT.

The ITCZ exhibited a 27% larger rain rate diurnal cycle and a 29% larger PHC208 diurnal cycle amplitude (peak minus trough) than the equatorial region with the most significant differences occurring in the morning. (Percentages here are taken with respect to the lower value.) For rainfall, the mean rain rate was 0.34 mm/hr for the ITCZ and 0.27 mm/hr for the equatorial. The difference was greatest, around 0.11 mm/hr (33%), after sunrise, 0600–0900 LT (Figure 2a). In the evening the difference was much smaller, around 0.04 mm/hr (15%). Based on Student's *T* test, these results are significant at the 95% level. Similarly, for 208-K cloud coverage, the greatest difference is in the morning between 0300 and 0900 LT, which was noticeably greater than the difference at 1500–1800 LT. The maximum PHC difference of 0.4% was at 07 LT, which was 30% of the mean PHC magnitude at that hour. Note that while the EQ and ITCZ boxes have different sizes, both the rain rate and 208-K coverage are normalized by the area.

Similar to the diurnal cycle of radar rain rate, the TRMM MW diurnal cycle behaved differently for rain rates of 1–10 mm/hr and >10 mm/hr. For rain rates of 1–10 mm/hr, the frequency of occurrence had a

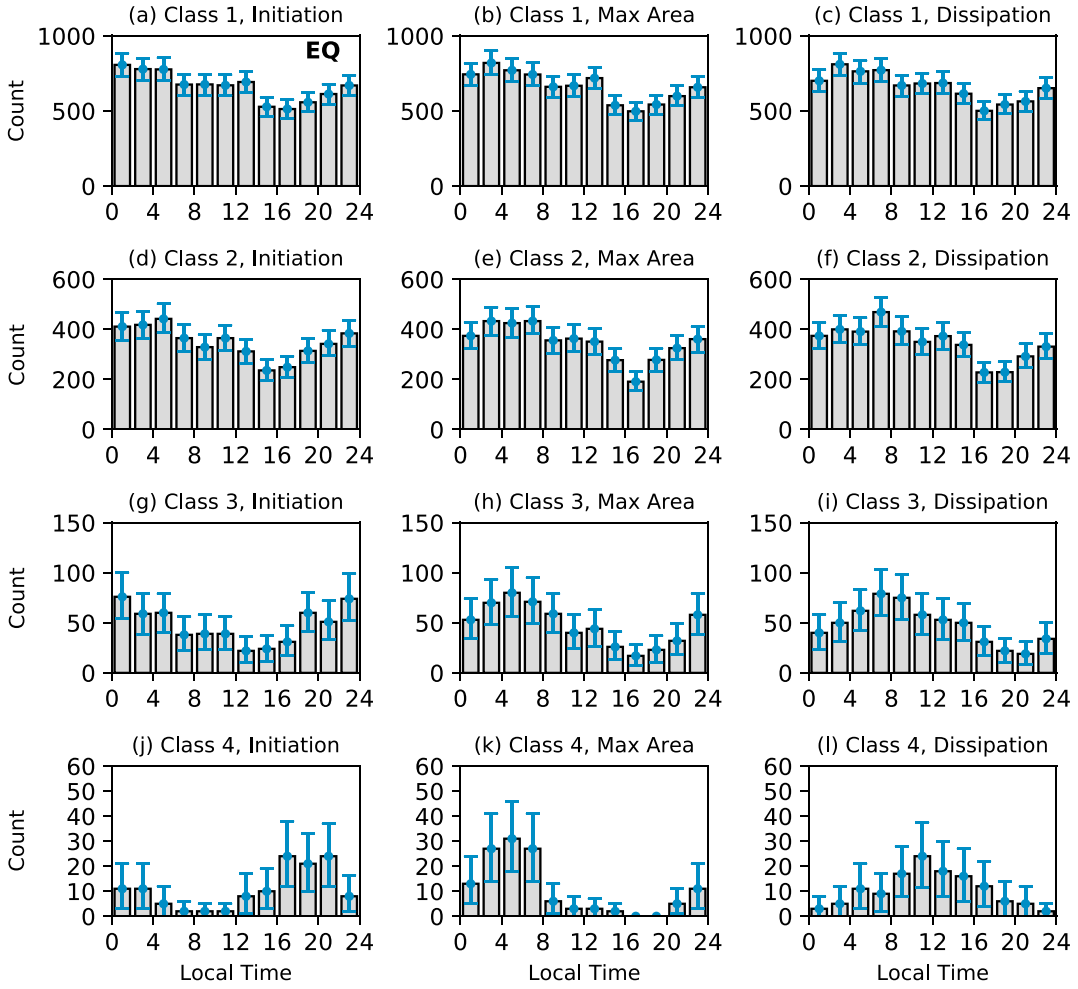

Figure 14. Diurnal life cycle of time clusters for the equatorial (EQ) region. Local time of (a) Initiation, (b) maximum area, and (c) dissipation of class 1 time clusters. Local time of (d) Initiation, (e) maximum area, and (f) dissipation of class 2 time clusters. Local time of (g) Initiation, (h) maximum area, and (i) dissipation of class 3 time clusters. Local time of (j) Initiation, (k) maximum area, and (l) dissipation of class 4 time clusters. Error bars represent the 95% confidence interval from bootstrap resampling (see text).

semidiurnal cycle with peaks at 0000–0300 LT and 1200–1500 LT (Figure 10). For rain rates >10 mm hr, the diurnal cycle peaked at 0000–0300 LT. Unlike the S-PolKa, SMART-R, and TOGA radar data, there was not a significant afternoon maximum in rain rates >10 mm/hr. The greatest rain rate contributions were from the heavier rain rates, leading to the overall TRMM MW diurnal maximum at 0000–0300 LT (Figure 11). In terms of the diurnal frequency of various rain rates, the notable difference between the equatorial and ITCZ regions was greater frequency of occurrence of >10 mm/hr rain rates especially in the morning.

In order to account for the regional morning rainfall differences illustrated in Figure 11, it is useful to look for differences in diurnal cycle partitioned by cloud cluster area. In terms of size dependent cloud cluster diurnal cycle, the greatest difference between the ITCZ and equatorial regions was for class for clusters during 0300–1200 LT (Figure 12c). To quantify the contribution of cloud clusters to the rainfall diurnal cycle, the TMPA grid cells overlapping the cloud clusters were identified and the rainfall was accumulated for those grid cells. Similar to the cloud cluster area, the rainfall produced by the class 4 clusters has the largest diurnal cycle (Figure 13). The morning diurnal peak for class 4 clusters is higher for the ITCZ than the EQ region. Differences between the ITCZ and equatorial regions suggest that similar to cold cloud area, the rainfall diurnal cycle difference during 0300–1200 LT is mostly related to the largest cloud clusters.

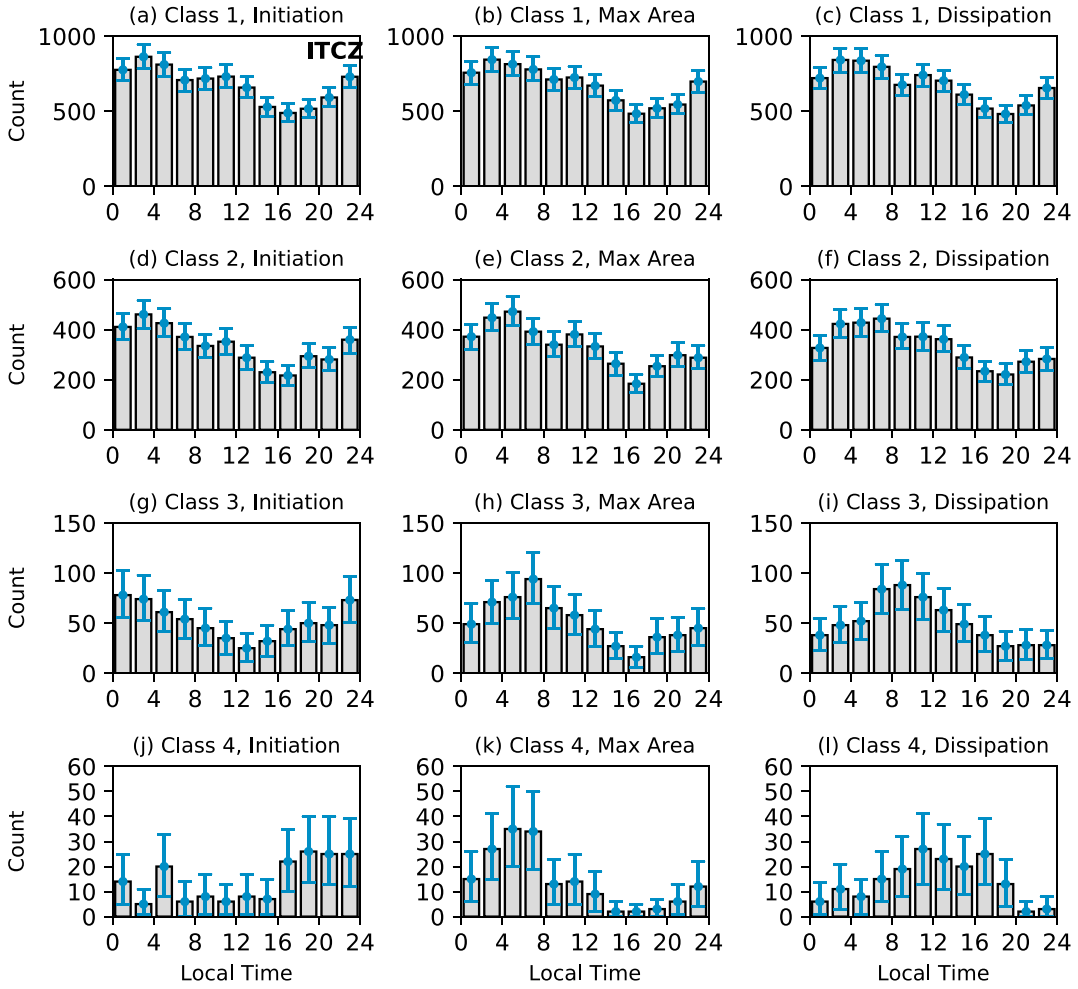

Figure 15. Same as Figure 14 but for the Intertropical Convergence Zone (ITCZ) region.

The largest cloud clusters are associated with large organized mesoscale convective systems with a distinct life cycle, which can be determined by tracking the cloud clusters in time. The next section explores the possible contribution of this life cycle to the diurnal cycle differences between the equatorial region and ITCZ.

6.2. Regional Diurnal Cycle Variability in Relation to the Life Cycle of Time Clusters

While small cloud systems go through their life cycles in a few hours, large, long-lasting time clusters can influence the diurnal cycle many hours after they initially develop. Class 1 and 2 clusters had their maximum initiation, peak area, and dissipation in the morning (Figures 14a–14f and 15a–15f). As indicated by the error bars, the diurnal variability is statistically significant at the 95% level. Note that unlike in CH97, the class 1 clusters do not have a midday maximum over the central IO, although they did plateau at midday. A similar analysis carried out over the western equatorial Pacific using the merged global IR data revealed a secondary afternoon maximum, consistent with CH97 (not shown). Class 3 clusters preferably initiated from 1800 to 0600 LT (Figures 14d and 15d). They tended to reach their maximum areal extent a few hours later (Figures 14e and 15e) and tended to dissipate around sunrise (Figures 14f and 15f). The timing of the diurnal cycle difference in cold clouds and rain is most correlated with the class 4 cluster contribution to the diurnal cycle (Figure 12), and the strongest diurnal life cycle is seen for the class 4 clusters (Figures 14g–14i and 15g–15i). Class 4 clusters had initiation peaks in the afternoon/evening, 1600–2200 LT for the equatorial region and 1600–0000 LT for the ITCZ (Figures 14g and 15g). The class 4 clusters reached their peak area at 0200–0600 LT in both the equatorial region the ITCZ (Figures 14h and 15h). However, there was a tendency of

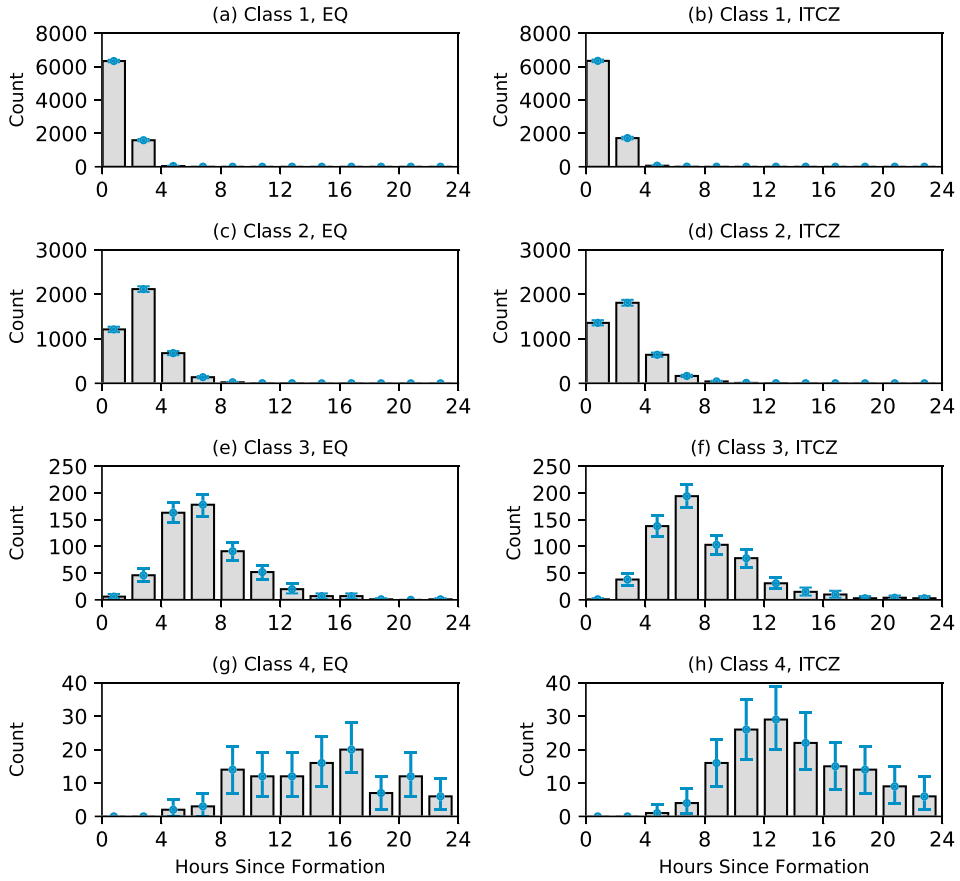

Figure 16. The duration of time clusters for (a) class 1 equatorial (EQ) region clusters, (b) class 1 Intertropical Convergence Zone (ITCZ) region clusters, (c) class 2 EQ region clusters, (d) class 2 ITCZ region clusters, (e) class 3 EQ region clusters, (f) class 3 ITCZ region clusters, (g) class 4 EQ region clusters, and (h) class 4 ITCZ region clusters. Error bars represent the 95% confidence interval from bootstrap resampling (see text).

more class 4 clusters reaching their maximum area at 0800–1400 LT in the ITCZ compared with the EQ region (significant at the 90% level). The later occurrence of initiation and peak area of the largest cloud clusters in the ITCZ is consistent with greater rainfall and cold cloud area in the morning in the ITCZ compared with the equatorial region (Figure 11). Dissipation for the class 4 clusters had a daytime maximum for both the equatorial region and ITCZ, but it had a more pronounced early morning peak in the equatorial region (Figures 14i and 15i).

The class 4 systems have the longest life cycle (Figure 16). Class 1 and 2 systems generally last $<$4 hr, although some class 2 systems last up to 7 hr. Class 3 systems most commonly lasted 4–7 hr and almost all $<$12 hr. These results are similar for both the equatorial region and ITCZ. However, the most significant difference between the equatorial region and ITCZ is with the class 4 systems. For the ITCZ, there are more class 4 systems lasting 8–15 hr (significant at the 90% level). This is consistent with the greater number of systems reaching their maximum size from 0600 to 1300 LT in the ITCZ (Figures 14k and 15k). It corresponds with the time of greatest difference between the equatorial region and ITCZ (Figures 11, 12c, and 13c).

The occurrence of more large, long-lived class 4 systems in the ITCZ is associated with greater and more continuous large-scale surface and low-level convergence compared with the equatorial region (Figure 17). In the equatorial region, the surface convergence (negative divergence) varies from 4 to 8 $\times$ 10^{-6} s^{-1} in active MJO periods to zero or marginally divergent during suppressed periods (Figure 17a). The Northern Sounding Array sounding divergence suggests that the surface divergence signal is representative of the lower troposphere (e.g., 1,000–800 hPa) and that large-scale divergence above the boundary layer in the

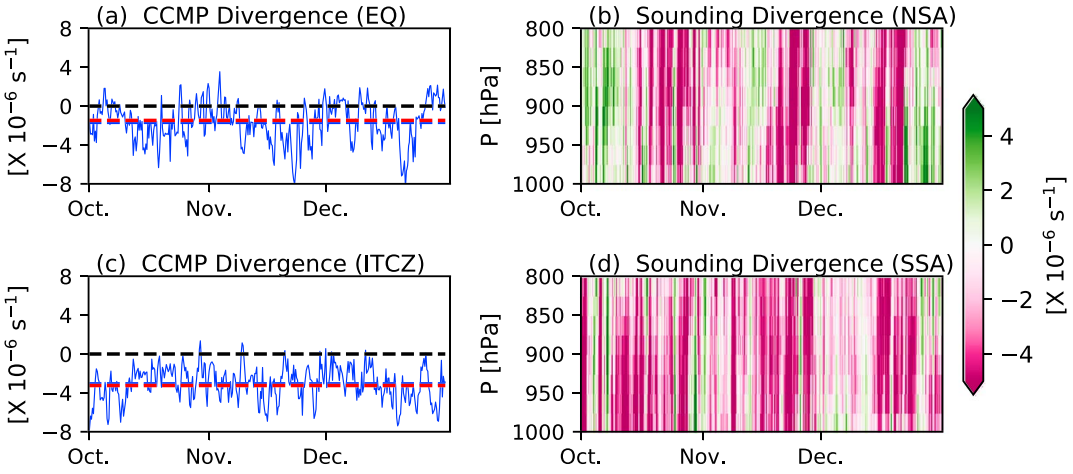

Figure 17. (a) Time series of surface wind divergence averaged over the equatorial (EQ) region for October to December 2011. (b) Time series of Northern Sounding Array (NSA) divergence with respect to pressure. (c) Time series of surface wind divergence averaged over the Intertropical Convergence Zone (ITCZ) region for October to December 2011. (b) Time series of Southern Sounding Array (SSA) divergence with respect to pressure. In (a) and (c), zero is indicated with a black dashed line, the October December 2011 mean with a dashed blue line, and the October to December 2007–2014 mean with a red dashed line. CCMP = Cross-calibrated Multiplatform.

equatorial suppressed phase can be substantial—up to 4 × 10^{-6} s^{-1} (Figure 17b). In contrast, the ITCZ experiences continuous large-scale surface convergence of 2–8 × 10–6 s^{-1} (Figure 17c). Within the Southern Sounding Array, the ITCZ large scale low-level convergence extends up to 800 hPa (Figure 17d). The mean surface convergence in the ITCZ is around twice that of the equatorial region (Figures 17a and 17c). The persistent ITCZ convergence is favorable for the development of large, organized convective cloud systems, which contribute more to the early morning rain maximum in the ITCZ than in the equatorial region. Large-scale forcing would generally be required to sustain convergence and convection over time scales of days to weeks, as mature mesoscale convective systems are associated with divergence and drying of the boundary layer, effectively sowing the seeds of their own demise (Houze, 1977, 2004; Simpson et al., 1967; Zipser, 1977). One mechanism proposed to sustain convection in the ITCZ is gradients in SST (Back & Bretherton, 2009; Carbone & Li, 2015). The SST gradient in the ITCZ is greater than in the EQ region; however, the largest SST gradients are located to the south of the ITCZ (Figure 1). This suggests that other factors contribute to the maintenance of ITCZ convection in the central IO.

7. Summary and Conclusions

This study documents differences in the diurnal cycle of precipitation in the MJO and ITCZ as estimated by radars and satellites (Figure 1). Similar to previous studies, the dominant diurnal cycle of rain and 208-K cold cloud tops is a nocturnal maximum (Figures 2, 10, and 11). Satellite and radar derived precipitation confirm the nighttime diurnal maximum in both the MJO and ITCZ over the IO. The data also reveal distinct characteristics between the two regions. The nighttime maximum in the ITCZ shifted more toward the morning than that of the equatorial region during the MJO (Figure 11). Satellite data shows that the greater morning rainfall in the ITCZ is associated with organized larger (>200 km) and long-lasting convective systems, consistent with the findings of CH97. The morning deep convection in the ITCZ increases low level divergence near the equator during the suppressed MJO (Ciesielski et al., 2018). ITCZ convection may play a role in delaying or preventing MJO onset when there is an active ITCZ. Kerns and Chen (2014) have proposed that when the ITCZ convection is diminished, it is more favorable for MJO initiation near the equator. Shipborne and island-based radar data show distinct characteristics of the diurnal cycle in the equatorial region and ITCZ, which has not been fully explored in previous studies.

Radar data show a secondary afternoon maximum in the equatorial IO when diurnal SST amplitude is relatively large ranging from 0.5 to 1.7 °C and surface wind speed is <5 m/s. This has been proposed to play

an important role in moisture preconditioning in advance of MJO initiation (Peatman et al., 2014; Ruppert & Johnson, 2015; Sakaeda et al., 2017). In contrast, the afternoon SST warming is mostly absent in ITCZ where wind speed is generally >5 m/s with a smaller SST diurnal cycle (Figure 2). The *Revelle* experienced periods of several days to weeks with surface wind speeds <5 m/s and daily afternoon SST maxima of 0.5–2.5 °C. While many of those days were suppressed and had little rain, especially days with SST maxima >1.7 °C, the days with rain tended to have an afternoon maximum (Figure 9). Although afternoon maxima were observed on some days by the *Mirai* radar, which sampled the ITCZ, most days were characterized by surface wind speeds >0.5 m/s, afternoon SST warming of <0.5 °C, and little rain. In summary, three diurnal cycle regimes were observed during DYNAMO:

1. Equatorial-MJO suppressed conditions: The day time warming of the SST is relatively large (> 0.5 °C) under weak winds (<5 m/s) and absent of wide spread convection, which may explain the observed afternoon peak in precipitation.
2. Equatorial-MJO active conditions: During active convection days the lower insolation and stronger surface winds (>5 m/s) reduce the afternoon SST warming, but convection may still be triggered in the afternoon and continue to grow into large and long-lasting systems in favorable convective environment, which results a nighttime precipitation and cold cloud tops maximum.
3. ITCZ: With persistent stronger winds and continuous confluence/convergence of the southeast trade winds, longer-lasting large convective systems are favored, which result in an even more pronounced night-morning precipitation and cold cloud tops maximum than that of the EQ.

While diurnal warming of the sea surface often led to afternoon convection and rainfall, there were several scenarios in which afternoon maxima did not occur. Under unfavorable, suppressed convective conditions with light winds near the equator, the afternoon SST maxima was >1.7 °C, but rain did not occur (Figures 4 and 9). Another scenario is that during periods with strong insolation and surface winds >5 m/s, SST warming was limited to <0.5 °C and forcing of afternoon convection was limited. Finally, when there is nocturnal morning convection, its remnants can prevent reinvigoration of afternoon convection the next day (i.e., *diurnal dancing*; Figures 8b and 8d).

The TMPA rainfall did not depict well the afternoon maximum of rain rates >10 mm/hr as shown by the equatorial region radars (see also Sakaeda et al., 2018), which are dominated by relatively isolated and small convective systems that are not well resolved by the TMPA data (Figures 11 and 14). The role of cloud clusters for the nocturnal maximum is explored using 8 years of overlapping IR satellite data and TMPA rainfall data. Cloud cluster tracking makes it possible to determine the role of large, long-lasting convective cloud systems and small, short-lived cloud systems for the diurnal cycle of rainfall, which is not feasible using radar data. Most of the climatological rain rate difference between the equatorial region and ITCZ was greater morning rainfall in the ITCZ. While the timing of the nocturnal maximum is similar for the EQ region and ITCZ, the amplitude of the diurnal cycle is 27% (29%) larger in terms of rain (cold clouds) for the ITCZ than of the equatorial region. The timing of the greatest ITCZ-EQ diurnal cycle difference in rainfall and 208-K IR cloud area are consistent—0300–1200 LT. The 208-K cloud and rainfall differences between the equatorial region and the ITCZ was accounted for mainly by the cold (208 K) cloud systems larger than 200 km (Figures 12 and 13). There were more of these large time clusters lasting 8–15 hr and reaching their maximum areal extent in the morning in the ITCZ (Figures 14, 15, and 16). The tendency of having more large, long-lasting cloud systems in the ITCZ is related to stronger and more persistent large-scale low-level convergence than in the equatorial region. These results show that diurnal air-sea forcing combined with the diurnal life cycle timing of large, long-lasting convective systems can account for regional variability of the diurnal cycle over the open ocean.

Acknowledgments
This research is supported in part by the NSF DYNAMO Legacy Data project under grant AGS-1442095/1762255, the NASA PMM science team under grant NNX16AE40G/80NSSC18K0905, and the OVWST under grant NNX14AM78G/80NSSC18K0949. The radar, shipborne, and mooring data are from the DYNAMO Legacy data set that are available via an online user interface at http://dynamo.fl-ext.ucar.edu/dynamo_legacy/. The global IR satellite data are available from NASA DISC. TMPA data were obtained from the NASA TRMM/GPM program. CCMP version-2.0 vector wind analyses are produced by Remote Sensing Systems. Data are available at www.remss.com. Comments from three anonymous reviewers helped improve the manuscript.

References

Atlas, R., Hoffman, R. N., Ardizzone, J., Leidner, S. M., Jusem, J. C., Smith, D. K., & Gombos, D. (2011). A cross-calibrated, multiplatform ocean surface wind velocity product for meteorological and oceanographic applications. *Bulletin of the American Meteorological Society*, *92*(2), 157–174. https://doi.org/10.1175/2010BAMS2946.1

Back, L. E., & Bretherton, C. S. (2009). On the relationship between SST gradients, boundary layer winds, and convergence over the tropical oceans. *Journal of Climate*, *22*(15), 4182–4196. https://doi.org/10.1175/2009JCLI2392.1

Bowman, K. P., Collier, J. C., North, G. R., Wu, Q., Ha, E., & Hardin, J. (2005). Diurnal cycle of tropical precipitation in Tropical Rainfall Measuring Mission (TRMM) satellite and ocean buoy rain gauge data. *Journal of Geophysical Research*, *110*, D21104. https://doi.org/10.1029/2005JD005763

Carbone, R. E., & Li, Y. (2015). Tropical oceanic rainfall and sea surface temperature structure: Parsing causation from correlation in the MJO. *Journal of the Atmospheric Sciences*, *72*(7), 2703–2718. https://doi.org/10.1175/JAS-D-14-0226.1

Chen, S. S., & Houze, R. A. (1997). Diurnal variation and life-cycle of deep convective systems over the tropical pacific warm pool. *Quarterly Journal of the Royal Meteorological Society*, *123*(538), 357–388. https://doi.org/10.1002/qj.49712353806

Chen, S. S., Houze, R. A., & Mapes, B. E. (1996). Multiscale variability of deep convection in relation to large-scale circulation in TOGA COARE. *Journal of the Atmospheric Sciences*, *53*(10), 1380–1409. https://doi.org/10.1175/1520-0469(1996)053<1380:MVODCI>2.0.CO;2

Chen, S. S., Kerns, B. W., Guy, N., Jorgensen, D. P., Delanoë, J., Viltard, N., et al. (2016). Aircraft observations of dry air, ITCZ, convective cloud systems and cold pools in MJO during DYNAMO. *Bulletin of the American Meteorological Society*, *97*(3), 405–423. https://doi.org/10.1175/BAMS-D-13-00196.1

Ciesielski, P. E., Johnson, R. H., Schubert, W. H., Ruppert, J. H., Ciesielski, P. E., Johnson, R. H., et al. (2018). Diurnal cycle of the ITCZ in DYNAMO. *Journal of Climate*, *31*(11), 4543–4562. https://doi.org/10.1175/JCLI-D-17-0670.1

Ciesielski, P. E., Johnson, R. H., Yoneyama, K., & Taft, R. K. (2014). Mitigation of Sri Lanka Island effects in Colombo sounding data and its impact on DYNAMO analyses. *Journal of the Meteorological Society of Japan*, *92*(4), 385–405. https://doi.org/10.2151/jmsj.2014-407

Ciesielski, P. E., Yu, H., Johnson, R. H., Yoneyama, K., Katsumata, M., Long, C. N., et al. (2014). Quality-controlled upper-air sounding dataset for DYNAMO/CINDY/AMIE: Development and corrections. *Journal of Atmospheric and Oceanic Technology*, *31*(4), 741–764. https://doi.org/10.1175/JTECH-D-13-00165.1

Cox, S. K., & Griffith, K. T. (1979). Estimates of radiative divergence during phase III of the GARP Atlantic tropical experiment: Part II. Analysis of phase III results. *Journal of the Atmospheric Sciences*, *36*(4), 586–601. https://doi.org/10.1175/1520-0469(1979)036<0586:EORDDP>2.0.CO;2

Dai, A. (2001). Global precipitation and thunderstorm frequencies. Part II: Diurnal variations. *Journal of Climate*, *14*(6), 1112–1128. https://doi.org/10.1175/1520-0442(2001)014<1112:GPATFP>2.0.CO;2

Dudhia, J. (1989). Numerical study of convection observed during the winter monsoon experiment using a mesoscale two-dimensional model. *Journal of the Atmospheric Sciences*, *46*(20), 3077–3107. https://doi.org/10.1175/1520-0469(1989)046<3077:NSOCOD>2.0.CO;2

Gottschalck, J., Roundy, P. E., Schreck, C. J. III, Vintzileos, A., & Zhang, C. (2013). Large-scale atmospheric and oceanic conditions during the 2011–12 DYNAMO field campaign. *Monthly Weather Review*, *141*(12), 4173–4196. https://doi.org/10.1175/MWR-D-13-00022.1

Gray, W. M., & Jacobson, R. W. (1977). Diurnal variation of deep cumulus convection. *Monthly Weather Review*, *105*(9), 1171–1188. https://doi.org/10.1175/1520-0493(1977)105<1171:DVODCC>2.0.CO;2

Houze, R. A. (1977). Structure and dynamics of a tropical squall–line system. *Monthly Weather Review*, *105*(12), 1540–1567. https://doi.org/10.1175/1520-0493(1977)105<1540:SADOAT>2.0.CO;2

Houze, R. A. (2004). Mesoscale convective systems. *Reviews of Geophysics*, *42*, RG4003. https://doi.org/10.1029/2004RG000150

Huffman, G. J., Bolvin, D. T., Nelkin, E. J., Wolff, D. B., Adler, R. F., Gu, G., et al. (2007). The TRMM Multisatellite Precipitation Analysis (TMPA): Quasi-global, multiyear, combined-sensor precipitation estimates at fine scales. *Journal of Hydrometeorology*, *8*(1), 38–55. https://doi.org/10.1175/JHM560.1

Ichikawa, H., & Yasunari, T. (2006). Time–space characteristics of diurnal rainfall over Borneo and surrounding oceans as observed by TRMM-PR. *Journal of Climate*, *19*(7), 1238–1260. https://doi.org/10.1175/JCLI3714.1

Janowiak, J. E., Arkin, P. A., Morrissey, M., Janowiak, J. E., Arkin, P. A., & Morrissey, M. (1994). An examination of the diurnal cycle in oceanic tropical rainfall using satellite and in situ data. *Monthly Weather Review*, *122*(10), 2296–2311. https://doi.org/10.1175/1520-0493(1994)122<2296:AEOTDC>2.0.CO;2

Janowiak, J. E., Joyce, R. J., & Yarosh, Y. (2001). A real–time global half–hourly pixel–resolution infrared dataset and its applications. *Bulletin of the American Meteorological Society*, *82*(2), 205–217. https://doi.org/10.1175/1520-0477(2001)082<0205:ARTGHH>2.3.CO;2

Johnson, R. H., Ciesielski, P. E., Ruppert, J. H., & Katsumata, M. (2015). Sounding-based thermodynamic budgets for DYNAMO. *Journal of the Atmospheric Sciences*, *72*(2), 598–622. https://doi.org/10.1175/JAS-D-14-0202.1

Judt, F., & Chen, S. S. (2014). An explosive convective cloud system and its environmental conditions in MJO initiation observed during DYNAMO. *Journal of Geophysical Research: Atmospheres*, *119*, 2781–2795. https://doi.org/10.1002/2013JD021048

Kerns, B. W., & Chen, S. S. (2014). Equatorial dry air intrusion and related synoptic variability in MJO initiation during DYNAMO. *Monthly Weather Review*, *142*(3), 1326–1343. https://doi.org/10.1175/MWR-D-13-00159.1

Li, Y., Han, W., Shinoda, T., Wang, C., Lien, R. C., Moum, J. N., & Wang, J. W. (2013). Effects of the diurnal cycle in solar radiation on the tropical Indian Ocean mixed layer variability during wintertime Madden-Julian Oscillations. *Journal of Geophysical Research: Oceans*, *118*, 4945–4964. https://doi.org/10.1002/jgrc.20395

Lukas, R., & Lindstrom, E. (1991). The mixed layer of the western equatorial Pacific Ocean. *Journal of Geophysical Research*, *96*(S01), 3343. https://doi.org/10.1029/90JC01951

Lutz, J., Johnson, P., Lewis, B., Loew, E., Randall, M., & Van Andel, J. (1995). NCAR SPol: Portable polarimetric S-band radar. Preprints, Ninth Symp. on Meteorological Observations and Instrumentation (pp. 408-410). Charlotte, NC: American Meteor Society.

Mapes, B. E., Warner, T. T., Xu, M., & Negri, A. J. (2003). Diurnal patterns of rainfall in northwestern South America. Part I: Observations and context. *Monthly Weather Review*, *131*(5), 799–812. https://doi.org/10.1175/1520-0493(2003)131<0799:DPORIN>2.0.CO;2

Matthews, A. J., Baranowski, D. B., Heywood, K. J., Flatau, P. J., & Schmidtko, S. (2014). The surface diurnal warm layer in the Indian Ocean during CINDY/DYNAMO. *Journal of Climate*, *27*(24), 9101–9122. https://doi.org/10.1175/JCLI-D-14-00222.1

Mori, S., Jun-Ichi, H., Tauhid, Y. I., Yamanaka, M. D., Okamoto, N., Murata, F., et al. (2004). Diurnal land–sea rainfall peak migration over Sumatera Island, Indonesian maritime continent, observed by TRMM satellite and intensive rawinsonde soundings. *Monthly Weather Review*, *132*(8), 2021–2039. https://doi.org/10.1175/1520-0493(2004)132<2021:DLRPMO>2.0.CO;2

Nesbitt, S. W., & Zipser, E. J. (2003). The diurnal cycle of rainfall and convective intensity according to three years of TRMM measurements. *Journal of Climate*, *16*(10), 1456–1475. https://doi.org/10.1175/1520-0442(2003)016<1456:TDCORA>2.0.CO;2

Peatman, S. C., Matthews, A. J., & Stevens, D. P. (2014). Propagation of the Madden-Julian Oscillation through the Maritime Continent and scale interaction with the diurnal cycle of precipitation. *Quarterly Journal of the Royal Meteorological Society*, *140*(680), 814–825. https://doi.org/10.1002/qj.2161

Powell, S. W., & Houze, R. A. (2013). The cloud population and onset of the Madden-Julian Oscillation over the Indian Ocean during DYNAMO-AMIE. *Journal of Geophysical Research: Atmospheres*, *118*, 11,979–11,995. https://doi.org/10.1002/2013JD020421

Qian, J.-H., Robertson, A. W., & Moron, V. (2013). Diurnal cycle in different weather regimes and rainfall variability over Borneo associated with ENSO. *Journal of Climate*, *26*(5), 1772–1790. https://doi.org/10.1175/JCLI-D-12-00178.1

Ruppert, J. H., & Johnson, R. H. (2015). Diurnally modulated cumulus moistening in the preonset stage of the Madden–Julian Oscillation during DYNAMO*. *Journal of the Atmospheric Sciences*, *72*(4), 1622–1647. https://doi.org/10.1175/JAS-D-14-0218.1

Sakaeda, N., Kiladis, G., & Dias, J. (2017). The diurnal cycle of tropical cloudiness and rainfall associated with the Madden-Julian Oscillation. *Journal of Climate*, *30*(11), 3999–4020. https://doi.org/10.1175/JCLI-D-16-0788.1

Sakaeda, N., Powell, S. W., Dias, J., & Kiladis, G. N. (2018). The diurnal variability of precipitating cloud populations during DYNAMO. *Journal of the Atmospheric Sciences*, *75*(4), 1307–1326. https://doi.org/10.1175/JAS-D-17-0312.1

Simpson, J., Garstang, M., Zipser, E. J., & Dean, G. A. (1967). A study of a non-deepening tropical disturbance. *Journal of Applied Meteorology*, *6*(2), 237–254. https://doi.org/10.1175/1520-0450(1967)006<0237:ASOAND>2.0.CO;2

Tao, W.-K., Lang, S., Simpson, J., Sui, C.-H., Ferrier, B., & Chou, M.-D. (1996). Mechanisms of cloud-radiation interaction in the tropics and midlatitudes. *Journal of the Atmospheric Sciences*, *53*(18), 2624–2651. https://doi.org/10.1175/1520-0469(1996)053<2624:MOCRII>2.0.CO;2

Tian, B., Waliser, D. E., & Fetzer, E. J. (2006). Modulation of the diurnal cycle of tropical deep convective clouds by the MJO. *Geophysical Research Letters*, *33*, L20704. https://doi.org/10.1029/2006GL027752

Tropical Rainfall Measuring Mission (TRMM) (2011). TRMM (TMPA) Rainfall Estimate L3 3 hour 0.25 degree x 0.25 degree V7, Greenbelt, MD, Goddard Earth Sciences Data and Information Services Center (GES DISC). https://dpoi.org/10.5067/TRMM/TMPA/3H/7 (Accessed: 1 December 2017).

UCAR/NCAR - Earth Observing Laboratory (1996). S-PolKa: S-band/Ka-band Dual Polarization, Dual Wavelength Doppler Radar. UCAR/NCAR - Earth Observing Laboratory. https://doi.org/10.5065/D6RV0KR8 (Retrieved 16 March 2017).

Webster, P. J., & Stephens, G. L. (1980). Tropical upper-tropospheric extended clouds: Inferences from winter MONEX. *Journal of the Atmospheric Sciences*, *37*(7), 1521–1541. https://doi.org/10.1175/1520-0469-37.7.1521

Wentz, F. J., Scott, J., Hoffman, R., Leidner, M., Atlas, R., & Ardizzone, J. (2015). Remote Sensing Systems Cross-Calibrated Multi-Platform (CCMP) 6-hourly ocean vector wind analysis product on 0.25 deg grid, Version 2.0. Remote Sensing Systems, Santa Rosa, CA. Retrieved from www.remss.com/measurements/ccmp. (Accessed 1 February 2018).

Williams, M., & Houze, R. A. (1987). Satellite-observed characteristics of winter monsoon cloud clusters. *Monthly Weather Review*, *115*(2), 505–519. https://doi.org/10.1175/1520-0493(1987)115<0505:SOCOWM>2.0.CO;2

Yang, G. Y., & Slingo, J. (2001). The diurnal cycle in the tropics. *Monthly Weather Review*, *129*(4), 784–801. https://doi.org/10.1175/1520-0493(2001)129<0784:TDCITT>2.0.CO;2

Yokoi, S., Katsumata, M., & Yoneyama, K. (2014). Variability in surface meteorology and air-sea fluxes due to cumulus convective systems observed during CINDY/DYNAMO. *Journal of Geophysical Research*, *119*, 2064–2078. https://doi.org/10.1002/2013JD020621

Yoneyama, K., Zhang, C., & Long, C. N. (2013). Tracking pulses of the Madden-Julian Oscillation. *Bulletin of the American Meteorological Society*, *94*(12), 1871–1891. https://doi.org/10.1175/BAMS-D-12-00157.1

Yuter, S. E., & Houze, R. A. (1995). Three-dimensional kinematic and microphysical evolution of Florida cumulonimbus. Part II: Frequency distributions of vertical velocity, reflectivity, and differential reflectivity. *Monthly Weather Review*, *123*(7), 1941–1963. https://doi.org/10.1175/1520-0493(1995)123<1941:TDKAME>2.0.CO;2

Zipser, E. J. (1977). Mesoscale and convective-scale downdrafts as distinct components of squall-line structure. *Monthly Weather Review*, *105*(12), 1568–1589. https://doi.org/10.1175/1520-0493(1977)105<1568:MACDAD>2.0.CO;2

Zuluaga, M. D., & Houze, R. A. (2013). Evolution of the population of precipitating convective systems over the equatorial Indian Ocean in active phases of the Madden–Julian Oscillation. *Journal of the Atmospheric Sciences*, *70*(9), 2713–2725. https://doi.org/10.1175/JAS-D-12-0311.1